



UNICA

UNIVERSITÀ
DEGLI STUDI
DI CAGLIARI



Università di Cagliari

UNICA IRIS Institutional Research Information System

This is the Author's manuscript version of the following contribution:

Antimony contamination sources and alteration pathways of Sb mineral phases in an abandoned mining area: The role of secondary mopungite [NaSb(OH)₆]

Dario Fancello ^a, Elisabetta Dore ^{a,*}, Daniela Medas ^a, Nicola Rigonat ^a, Carlo Meneghini ^b, Marilena Moroni ^c, Stefano Naitza ^a, Patrizia Onnis ^d, Giovanni De Giudici ^a

^a Department of Chemical and Geological Sciences, University of Cagliari, Cittadella Universitaria, Monserrato, 09042, CA, Italy

^b Department of Science, Roma Tre University, Rome, Italy

^c Department of Earth Sciences, University of Milan, Italy

^d Environment & Sustainability Institute and Camborne School of Mines, University of Exeter, Penryn, TR10 9FE, United Kingdom

The publisher's version is available at:

<https://doi.org/10.1016/j.apgeochem.2023.105764>

When citing, please refer to the published version.

Antimony contamination sources and alteration pathways of Sb mineral phases in an abandoned mining area: the role of secondary mopungite [NaSb(OH)₆]

Dario Fancello^a, Elisabetta Dore^{a*}, Daniela Medas^a, Nicola Rigonat^a, Carlo Meneghini^b, Marilena Moroni^c, Stefano Naitza^a, Patrizia Onnis^d, Giovanni De Giudici^a

^aDepartment of Chemical and Geological Sciences, University of Cagliari, Cittadella Universitaria, Monserrato, 09042, CA, Italy

^bDepartment of Science, Roma Tre University, Rome, Italy

^cDepartment of Earth Sciences, University of Milan, Italy

^dEnvironment & Sustainability Institute and Camborne School of Mines, University of Exeter, Penryn, TR10 9FE, United Kingdom

Correspondence: Elisabetta Dore (elisabetta.dore@unica.it)

ABSTRACT

Antimony pollution caused by mining activities is a current environmental concern. This study investigates the processes involved in the Sb release and mobility in the abandoned Sb mine of Su Suergiu (SE Sardinia, Italy). Analyses of outcropping rocks, mine wastes and foundry slags by means of X-Ray Powder Diffraction, Scanning Electron Microscopy - Energy Dispersive Spectroscopy and Electron Microprobe – Wavelength Dispersive Spectroscopy provided mineralogical and compositional data which contributed to the discussion about the oxidation pathways of Sb phases. The main Sb sources are metallic Sb and Sb₂O₃ (valentinite/sénarmontite), dumped in the foundry slag heaps as residues of metallurgical processes, and primary stibnite (Sb₂S₃) found in natural outcrops and mine wastes. These minerals, subjected to weathering processes, release Sb in solution where it is oxidized and remains as dissolved Sb(OH)₆⁻. Carbonates and Na phases, like hydrate NaAl-silicate derived from metallurgical processes, influence the geochemical equilibria of the foundry slag heaps, where the precipitation of the rare mopungite, Na[Sb(OH)₆], has been observed. At Su Suergiu, mopungite originates from a dissolution-precipitation process as the last forming mineral of the oxidation pathways, limiting the Sb mobility by bonding the Sb(OH)₆⁻ in solution. Among the detected Sb secondary phases (e.g., Sb-oxides, FeSb-oxides, etc.), mopungite is the main Sb binder although it acts as a temporary sink because its stability is influenced by the hydrological regime, its solubility, and the water physicochemical parameters. Secondary Sb-bearing minerals can control the dispersion of Sb in contaminated area. At Su Suergiu the role of Fe-bearing compounds on Sb mobility is subordinate to that of mopungite due to the specific geochemical conditions linked to the metallurgical activities. The relevance of this study arises from the worldwide diffuse Sb mining, being in the top ten of the most mined elements worldwide, its toxicity and widespread

35 occurrence of Na-Sb-rich residues produced by Sb smelting plants.

36
37 **Keywords:** antimony mine, mopungite, Sb pollution, secondary minerals

38 39 **1. Introduction**

40 Antimony (Sb) is a non-essential element, and it is considered a potential human carcinogen.
41 Although the knowledge about the toxicity of Sb compounds for the ecosystem is still lacking, high
42 Sb concentrations are considered a serious environmental and health concern (Bagherifam et al.,
43 2021; Filella et al., 2009; Gebel, 1997; Gurnani et al., 1994; He et al., 2019). For these reasons in the
44 last decades Sb has gained environmental interest and, the World Health Organization (WHO, 2011)
45 and the European Community (European Commission, 1998) have set, respectively, the thresholds
46 of 20 $\mu\text{g L}^{-1}$ and 5 $\mu\text{g L}^{-1}$ of Sb concentration for drinking water.

47 Antimony concentration commonly ranges between 0.15 and 2 mg/kg in most rocks and it is usually
48 below 1 $\mu\text{g/L}$ in uncontaminated freshwaters (Filella et al., 2002b). Higher Sb concentrations in the
49 environment can be due to both natural and anthropogenic sources, such as volcanism and ore
50 minerals, shooting ranges, agricultural activities, transports, mining etc. (Hayes & Jr., 1991; He et al.,
51 2019; Ngo et al., 2020; Okkenhaug et al., 2016). Being Sb in the top ten of the most mined elements
52 worldwide, mining exploitation and foundry activities are supposed to be the greatest sources of Sb
53 in the environment (Mitsunobu et al. 2009; Álvarez-Ayuso et al. 2013 and reference therein). These
54 activities unearth ore minerals exposing them to oxidation, and produces huge volumes of highly
55 polluting wastes such as primary ore, residues of metallurgical processes and secondary minerals
56 (Biver & Shotyk, 2013; Filella et al., 2009; Ilgen et al., 2014; Multani et al., 2016). The reactivity of
57 these materials, when exposed to surface/near surface conditions, depends on their mineralogical
58 composition (Álvarez-Ayuso et al., 2013; Ashley et al., 2006; Cidu et al., 2018; He et al., 2019;
59 Majzlan et al., 2011, and references therein), thus their characterization is fundamental to understand
60 the processes occurring in mine areas and to evaluate the mechanisms leading to Sb release in a
61 specific environment (Borčinová Radková et al., 2020; Courtin-Nomade et al., 2012; Filella, 2011;
62 Filella et al., 2009; Roper et al., 2012; Wilson et al., 2004).

63 Antimony ore deposits are usually connected to hydrothermal activities where the primary ore is
64 stibnite (Sb_2S_3) (Fowler & Goering, 1991). Common primary Sb minerals are sulphides, whereas
65 oxides and sulphosalts may form especially in sulphur-deficient environment (Roper et al., 2012).
66 Primary Sb sulphides are relatively insoluble at ambient temperature (Multani et al., 2016) however,
67 in oxygen-rich environment, they tend to change to Sb(III) oxides that are further oxidized to Sb(V),

68 thereby allowing the Sb release in solution (Borčinová Radková et al., 2020). Weathering phases of
69 stibnite oxidation are kermesite ($\text{Sb}_2\text{S}_2\text{O}$), sénarmontite/valentinite (Sb_2O_3) and stibiconite
70 ($\text{Sb}_3\text{O}_6\text{OH}$) (Roper et al., 2012) plus other oxides, sulfosalts and hydroxides, the presence of which
71 depends on the geological setting and local geochemical conditions (like circulating solutions
72 enriched in Ca^{2+} , Pb^{2+} , Fe^{3+} , etc.) (Borčinová Radková et al., 2020, 2022; Majzlan et al., 2016).

73 In mine areas where residues of mining excavation are dumped together with tailings and residues of
74 metallurgy, the oxidation pathways of Sb minerals become more complex. As an instance, tailings
75 residual from flotation plants, still contain Sb and other elements commonly associated in primary
76 ores (As, Fe, Pb, Zn, etc.), together with reagents used in flotation processes (Long et al., 2020;
77 Multani et al., 2016). In addition, different metallurgical processes require the use of carbonates,
78 alkali and other reagents that produce large amounts of complex wastes (Multani et al., 2016 and
79 references therein). Several studies demonstrated that the potential to release toxic elements by these
80 wastes depends on their mineralogy rather than their bulk chemistry (Guo et al., 2014; Majzlan et al.,
81 2011; Su et al., 2021).

82 Secondary Sb(V) minerals may limit Sb dispersion and/or mobility in function of local geochemical
83 condition and mineral solubility; minerals like the roméite group and tripuhyite (Roper et al. 2015
84 and references therein; Leverett et al. 2012) can incorporate Sb(V) in their structure in a stable way,
85 whereas other phases like minerals with general formula $\text{M}^{\text{x}+}[(\text{Sb}(\text{OH})_6)_x \cdot m\text{H}_2\text{O}]$ ($\text{M}^{\text{x}+} = \text{Ca}^{2+}$, Na^+ ,
86 Mg^{2+} etc.) like brandholzite $[\text{Mg}(\text{H}_2\text{O})_6(\text{Sb}(\text{OH})_6)_2]$ and $\text{Ca}[\text{Sb}(\text{OH})_6]_2$, might limit Sb mobility only
87 temporarily (Diemar et al., 2009; Friedrich et al., 2000; Sejkora et al., 2010; Borčinová Radková et
88 al., 2020; Johnson et al., 2005; Okkenhaug et al., 2011). Among these minerals, mopungite,
89 $\text{Na}[\text{Sb}(\text{OH})_6]$, a rare naturally occurring mineral, was detected in some sites either as a result of
90 stibnite alteration in surface environment (Bittarello et al., 2015; Marzoni Fecia Di Cossato et al.,
91 1987; Roper et al., 2018; Williams, 1985) or as a possible product of the interaction between primary
92 Sb ore and reagents employed in the mineral processing (Protano and Riccobono, 1997). Roper et al.
93 (2018) indicated that mopungite can exist as a precursor of brizzite (NaSbO_2), however studies
94 focused on the role of mopungite on Sb mobility in mine areas are still lacking.

95 This work is set in the abandoned Sb mine area of Su Suergiu (SE Sardinia, Italy) affected by serious
96 Sb pollution, whose drainages impact the water bodies up to several kilometres downstream hence
97 affecting the most important river (Flumendosa River) of SE Sardinia (Cidu et al., 2014, 2018). This
98 work aims to shed light on the processes involved in the fate of Sb at the contamination sources. For
99 this purpose, the mineralogy and chemistry of outcropping rocks, mine wastes and residues of
100 metallurgical processes have been studied combining laboratory and synchrotron radiation X-Ray
101 Powder Diffraction (XRD), Scanning Electron Microscopy - Energy Dispersive Spectroscopy (SEM-

102 EDS) and Electron Microprobe – Wavelength Dispersive Spectroscopy (EMP-WDS) to identify the
103 Sb primary and secondary phases and to reconstruct the oxidation pathways. This study deepens the
104 knowledge on Sb behaviour in mine-impacted areas and represents a useful tool in planning
105 remediation actions, not only at Su Suergiu but also in other Sb mines worldwide.

106
107

2. Study area

108

2.1 Geological setting and mine history

109

110 The Su Suergiu abandoned mine is located in the Gerrei mine district (SE Sardinia, Italy) (Fig. 1 a-
111 c). The geology of the region is characterized by low-grade metamorphic rocks belonging to
112 allochthonous units emplaced during the Variscan orogenesis (Carmignani et al., 2001). The weakly
113 metamorphosed outcropping succession consists of Cambrian to Lower Ordovician siliciclastic
114 deposits followed by Middle-Late Ordovician volcanics and siliciclastic rocks, Silurian-Middle
115 Devonian black shales and limestones, Middle Devonian-Lower Carboniferous limestones and Lower
116 Carboniferous Culm-type deposits (Fig. 1c, RAS 2013).

117

118 The mineralization of Su Suergiu resulted from hydrothermal activity related to the late Variscan
119 extensional tectonics (Funedda et al., 2018). The deposit mainly consists of sulphides- and scheelite
120 [Ca(WO₄)]-bearing lenses and veins that follow the main foliation of highly deformed black shales
121 and metalimestones belonging to the cataclastic Villasalto thrust zone (Carmignani et al., 1978). In
122 detail, the ore mined at Su Suergiu is mainly made up by stibnite, arsenopyrite (FeAsS), scheelite,
123 pyrite (FeS₂), with minor amounts of sphalerite (ZnS), chalcopyrite (CuFeS₂), berthierite (FeSb₂S₄),
124 marcasite (FeS₂), pyrrhotite (FeS), tetrahedrite [(Cu,Fe,Ag,Zn)₁₂(Sb,As)₄S₁₃], galena (PbS),
125 boulangerite (Pb₅Sb₄S₁₁), native gold (Au) and native antimony (Sb), in calcite (CaCO₃) and quartz
126 (SiO₂) gangue (Funedda et al., 2005).

127

128 The Su Suergiu deposit was mined underground from 1880 to 1960, with an exploitation peak
129 between the 1920's and 1930's. The foundry operated from 1882 to 1981, with alternating periods of
130 stop and restart, processing local ores and, after the mine closure in 1960's, Sb-ores coming from
131 Tuscany, China and Bolivia (Amat di San Filippo, 2014; Cidu et al., 2018; Contini et al., 2009; Secchi
132 & Lorrain, 2001). In the early years of activity, the main products of the plant were liquated sulphide
133 (Sb₂S₃) and Sb oxide (Sb₂O₃). From the first decade of XXth century, the foundry also produced
134 metallic Sb (Contini et al., 2009; Secchi & Lorrain, 2001). In the first step of the process, carbonate
135 gangue, metallurgical coke, flue dust and searing charcoal were added to Sb ore in the converters.

136

137 During the reduction processes to obtain metallic Sb from the oxide, the reverberatory furnaces were
138 charged with a mixture of oxide and charcoal with the addition of Na-carbonate as fluxing agent in

139
140
141
142
143
144
145

135 the percentage of 3.5% (Amat di San Filippo, 2014).
136 Waste materials deriving from the underground exploitation (hereafter referred to as mine waste) and
137 residues of metallurgical processes (hereafter referred to as foundry slags) were dumped within the
138 mine area (Fig. 2). When the mining and foundry activities definitively ceased, no actions addressed
139 to mitigate the contamination were realized due to the lack of environmental legislation. In the mine
140 area 14 mine waste dumps, for a total of 146,308 m³ (IGEA, 2009), have been identified (Fig. 2).
141 They are mostly covered by vegetation and they show evidence of erosional processes only close to
142 the streams. The foundry slags, consisting of vacuolar slags, massive glass slags, rotary furnace slags
143 and various casting remains, were dumped in two main bodies (65,460 m³), which also contain minor
144 amount of mine waste (Fig. 2) (Contini et al., 2009; IGEA, 2009). In this case the vegetation is absent
145 and, despite the presence of retaining walls on the heaps edge, the foundry slag heaps have been
146 subjected to considerable erosion, especially during episodic extreme hydrological events. It has been
147 estimated that about 18,400 m³ (IGEA, 2009) of these wastes are accumulated along the riverbank
148 downstream the mine area up to the Flumendosa River.

2.2 Characteristics of the area and water geochemistry

151 The climate of the area is semi-humid with dry summers and variable rainfall mainly distributed from
152 October to April; the mean annual temperature and precipitations, based on data collected from 1955
153 to 1992, are 16°C and 670 mm, respectively (RAS, 1998).

154 The hydrology of the mine area is characterized by intermittent streams whose flow is strictly
155 dependent on rainfall. The mine area is drained by Riu Su Suergiu, whose waters flow into the Riu
156 Ciurixeda catchment (Figs. 1c and 2) which, in turn, flow untreated into the Flumendosa River, the
157 main river of SE Sardinia, used for agricultural and human consumptions.

158 Several hydrogeochemical surveys (from 2005 to 2015) were carried out over an area comprising the
159 Su Suergiu mine area, the Riu Ciurixeda catchment and a portion of the Flumendosa River (before
160 and after the confluence of Riu Ciurixeda).

161 These studies showed that waters flowing in the mine area are characterized by a Ca(Na)-sulphate
162 composition, oxidizing conditions and neutral or slightly alkaline pH. The dissolution of sulphide
163 minerals produces high concentration of sulphate; this is an acidifying process, but the presence of
164 carbonates buffers the solution pH. The drainage flowing downstream the foundry slag heaps often
165 shows high Na concentration (up to 600 mg/L), probably as a consequence of the water interaction
166 with the alkaline materials used during the Sb-ore metallurgy (Cidu et al., 2021, 2018, 2014).

167 Data of water samples collected in the mine area between 2012 and 2014 showed a wide variability

168 of Sb concentrations (detailed information on samples location and Sb concentrations are reported in
169 Cidu et al., 2014). The highest values were determined in the slag drainage (up to 30,000 $\mu\text{g/L}$ Sb;
170 median value 13,000 $\mu\text{g/L}$ Sb), while in the other samples (adits, spring and streams) the Sb
171 concentration ranged between 48 – 4,020 $\mu\text{g/L}$ (median: 323 $\mu\text{g/L}$), thus indicating the foundry slag
172 heaps as the main source of dissolved Sb.

173 After the confluence with Flumendosa River, water still shows Sb concentrations above the thresholds
174 set by the WHO (20 $\mu\text{g L}^{-1}$) (WHO, 2011) and the European Union (5 $\mu\text{g L}^{-1}$) (European Commission,
175 1998) for drinking water (Cidu et al., 2014, 2018). It was observed that, downstream the mine area,
176 the natural Sb attenuation occurs mainly by dilution whereas attenuation linked to adsorption or
177 precipitation of secondary Sb minerals has been considered negligible (Cidu et al., 2014, 2018).

178 It is noteworthy that also weathered mine wastes and foundry slag dispersed downstream the mine
179 area by runoff can contribute to increase dissolved Sb concentration in waters.

180

181

182

183

184

185

186

187

188

189

190

191

192

193

194

195

196

197

198

199

200

201

202

203

204

205

206

207

208

209

210

211

212

213

214

215

3. Materials and methods

3.1 Sampling and analyses

216 Different kinds of samples including outcropping rocks, mine wastes and foundry slags (Fig. 2), were
217 collected within the mine area to perform mineralogical (XRD) and minerochemical (SEM-EDS and
218 EMP-WDS) analyses. Further samples were collected along the Riu Su Suergiu riverbank, mainly
219 waste runoff downstream from the foundry slag heaps (Fig. 2).

220 After collection, samples were air-dried at room conditions. To perform XRD analysis, samples were
221 finely hand grinded in an agate mortar, then XRD patterns were acquired using a conventional θ - θ
222 equipment (PANalytical X'Pert Pro) with Cu K_{α} wavelength radiation (1.54060 Å) and a Ni filter,
223 operating at 40 kV and 40 mA, using the X'Celerator detector.

224 Selected samples were analysed at the MCX (Materials Characterisation X-ray diffraction) (Rebuffi
225 et al., 2014) line at the Elettra synchrotron light source (Basovizza, TS, Italy) using an incident
226 monochromatic beam with a wavelength of 0.95373 Å. XRD patterns were acquired using a step
227 scanning diffractometer in the 6-70° 2θ range with 0.012° 2θ step size. Sample powders were
228 mounted in thin windows glass capillaries that were kept spinning during acquisition to reduce
229 preferential orientation effects.

230 The phase identification was performed using the software X'Pert HighScore Plus (PANalytical B.V.,
231 Almelo, The Netherlands) following the previous steps of $K_{\alpha 2}$ stripping, trace smoothing and manual
232 peak finding. Rietveld structure refinement was performed using GSAS-II software (Toby & Von
233 Dreele, 2013) based on the mopingite structural file Sb07 from Palenik et al. (2005) and an iterative

201 process until the best values of Goodness of Fit (GoF) and wR were reached (Toby, 2006). The three-
202 dimensional structure visualization was performed using VESTA 3 software (Momma & Izumi,
203 2011) and the structural file built from the refined data using GSAS-II.

204 To better understand the relationship among the Sb-bearing phases detected by mineralogical analysis
205 and to assess the alteration path of Sb, SEM-EDS analysis was performed on different types of
206 foundry slag samples. SEM analysis was performed using a FEI Quanta 200 equipped with a
207 ThermoFisher UltraDry Energy EDS detector at the CeSAR laboratory (University of Cagliari).

208 Quantitative microanalyses were performed at the Dipartimento di Scienze della Terra (Università
209 Statale di Milano, Italy) by a JEOL JXA-8200 electron microprobe (EMP) equipped with five
210 wavelength-dispersive spectrometers (WDS). The list of analysed elements, with the relative
211 standards, spectral lines, and monochromators (in brackets) are here reported: Zn (Zn, K α , LIFH), Fe
212 (fayalite, K α , LIFH), Ni (nickeline, K α , LIFH), Co (Co, K α , LIFH), Mn (rhodonite, K α , LIFH), Sn
213 (Sn, L α , TAP), Sb (Sb, L α , TAP), Ca (grossular, K α , PETH), Si and Al (grossular, K α , TAP), Na
214 (omphacite, K α , TAP), K (K-feldspar, K α , PETH), Mg (olivine, K α , TAP), Ti (ilmenite, K α , PETJ),
215 Cr (Cr, K α , PETJ), W (W, L α , LIFH). The electron beam was set to 15 kV accelerating voltage, 5 nA
216 beam current, 1-2 μ m beam diameter, and each element was determined after counting time of 30
217 seconds on peak and 10 seconds on background. Element concentrations were determined after
218 applying $\phi(\rho z)$ algorithm and corrections for X-ray fluorescence, absorption, atomic number (Z) and
219 matrices, and by evaluating spectral interferences. The requirement of $I_{xstd}/I_{std} = 1.00 \pm 0.01$ was
220 checked for each element before the analysis (where, I_{xstd} intensity of the analysed standard, and I_{std}
221 the intensity of the same standard after calibration).

222 The Eh-pH diagrams were performed using the Hydra-Medusa software with its internal database
223 complex.db and complex.elb (Puigdomènech, 2010). The Hydra-Medusa database was modified
224 adding the solubility constant (K_s) of mopungite ($\log K_s$ -4.996) (Blandamer et al., 1974; Ilgen et al.,
225 2014). Concentrations used for the calculations were taken from Cidu et al., 2018, and Na and
226 $Sb(OH)_6^-$ values were varied to allow mopungite precipitation.

228 4. Results

229 4.1 XRD analysis and structural refinement

230 The mineralogical characterization reveals remarkable differences between the outcropping rocks,
231 the mine waste samples, and the foundry slags (Table 1).

232 In agreement with the geology of the study area, the mineralogy of outcropping rocks is mainly made
233 up by quartz and calcite with minor amounts of phyllosilicates, probably chlorite and/or illite and

234 muscovite (Table 1). Efflorescences and patinas were locally found onto the surface of natural
235 outcrops, resulting from the oxidation of metal-sulphides. These efflorescences mainly consist of
236 metal-sulphate hydrate as halotrichite ($\text{FeAl}_2(\text{SO}_4)_4 \cdot 22\text{H}_2\text{O}$), kalinite ($\text{KAl}(\text{SO}_4)_2 \cdot 11\text{H}_2\text{O}$), jarosite
237 ($\text{KFe}_3(\text{SO}_4)_2(\text{OH})_6$), plumbojarosite ($\text{Pb}_{0.5}\text{Fe}_3(\text{SO}_4)_2(\text{OH})_6$), hexahydrate ($\text{MgSO}_4 \cdot 6\text{H}_2\text{O}$) and other
238 sulphates with mixed metal cations and different hydration degree (Table 1, Fig. S1). However,
239 except some small amount of pyrite (Fig. S1), other sulphur-bearing phases related to the
240 mineralization event cannot be detected by XRD, likely due to their poor crystallinity and/or low
241 concentration.

242 The samples collected in the mine waste dumps show a mineralogical composition matching that of
243 the surrounding rock outcrops, since mine waste hosts the gangue and the overburden resulting from
244 excavation. The mineralogical composition consists of quartz, calcite, dolomite and phyllosilicates in
245 different proportions (Table 1 and Fig. S1). In some cases, the presence of the primary mineral stibnite
246 was observed; gypsum (and rarely hematite) is linked to the alteration of primary sulphides.

247 Slag samples collected at the foundry slag heaps show different colour, texture, consolidation degree
248 and a complex mineralogy attributable to the different metallurgical treatments employed during the
249 foundry activity and to the subsequent weathering processes (Table 1). Macroscopically, it is possible
250 to distinguish residues of rotary furnaces, casting residues and vacuolar or glassy massive slags, in
251 addition to metallic Sb (hereafter referred to as MET) found as encrustations on mould fragments
252 formerly used to cast the Sb ingots (Fig. 2).

253 The XRD patterns of samples representative of the different types of foundry slags are reported in
254 figure S1. The mineralogical composition of most samples consists of quartz, calcite, dolomite and
255 phyllosilicates belonging to the host rock; in some samples, minor amounts of ankerite
256 [$\text{Ca}(\text{Fe}^{2+}, \text{Mg})(\text{CO}_3)_2$] and arsenopyrite, probably derived from the primary mineralization are
257 detected (Table 1).

258 Diverse Na phases are commonly found as NaAl-silicate hydrate, NaAl-carbonate, and NaCa-sulfate
259 or carbonate. High-temperature minerals belonging to the sodalite-cancrinite group, as nosean
260 [$\text{Na}_8\text{Al}_6\text{Si}_6\text{O}_{24}(\text{SO}_4)$] and hauyne [$(\text{Na}, \text{Ca})_{4-8}\text{Al}_6\text{Si}_6(\text{O}, \text{S})_{24}(\text{SO}_4, \text{Cl})_{1-2}$], and mullite ($\text{Al}_{(4+2x)}\text{Si}_{(2-2x)}\text{O}_{(10-x)}$ where $x=0.17-0.59$) and cuspidine ($\text{Ca}_4\text{Si}_2\text{O}_7(\text{F}, \text{OH})_2$) rarely occur. The abundance of Na
261 minerals is attributable to the Na-rich additives employed in the reduction processes (mainly NaCO_3 :
262 Contini et al. 2009). The high-temperature silicates are byproducts of the foundry processes, where
263 the silica was probably provided by the gangue and, supposedly, from the quartz sand used for ingot
264 coating. The presence of cristobalite is also attributable to the high temperature of metallurgical
265 processes (Piatak & Ettl, 2021), as observed in the vitreous slags showing the typical background
266 of amorphous materials together with quartz and cristobalite peaks (e.g., sample SUMA 5_3, Fig.
267

268 S1).
269 Diverse Sb-bearing phases occur, such as metallic Sb or (rarely) metal alloy (Fe_2Sb), oxides
270 (sénarmontite, and valentinite, Sb_2O_3 ; rarely schafarzikite, FeSb_2O_4) and sulphides (tetrahedrite
271 $(\text{Cu,Fe})_{12}\text{Sb}_4\text{S}_{13}$) (Table 1, Fig. S1). Of particular interest is the diffused presence of mopungite
272 $\text{Na}[\text{Sb}(\text{OH})_6]$, always detected in the XRD patterns of altered casting residues and residues of rotary
273 furnaces. These samples often show crumbliness, powdery surfaces and patinas. Among them, two
274 samples of patinas scraped from highly altered casting residues (sample SUMA 5_6, Fig. 3a),
275 consisting of pure mopungite (Fig. S1), were analysed at the MCX line at the Elettra synchrotron light
276 source in order to perform the structural refinement. The obtained XRD patterns do not show peaks
277 of phases other than mopungite, the strongest reflections being $[\text{hkl} - d (\text{Å}) - (I)]: [(111 - 4.6 - 100)$
278 $(020 - 4.01 - 67) (022 - 2.81 - 36) (002 - 3.94 - 27.8)]$ (Figs. 3b and c). The structure of the analysed
279 samples belongs to the tetragonal system, space group $\text{P4}_2/\text{n}$, face-centered unit cell. The unit-cell
280 parameters obtained by the structural refinement are close to those reported by (Schrewelius, 1937),
281 and in general agreement with the more recent literature, slightly larger than those reported by Palenik
282 et al. (2005) and smaller than data from Bittarello et al. (2015) and Asai (1975). The results of the
283 Rietveld refinement and the structural parameters for the unit cell are reported in Table 2, whereas
284 the lists of reflections are reported in Tables S2 and S3.
285 The mineralogy of samples collected along the Rio Su Suergiu riverbank is quite similar to that of
286 the foundry slag heaps, but it is worth to note that, even if the samples are altered, the mopungite was
287 never detected (Table 1).

388 389 4.2 SEM and EMP analysis

390 SEM analyses performed on casting residues sampled at the foundry slag heaps, in agreement with
391 XRD results, show an elemental composition of the matrix (Si, Al, Ca, O, Na) compatible with the
392 presence of NaAl-silicate hydrate and calcite (Figs. 4 and 5). The local presence of Mg and Fe (sample
393 SUMA 5_7, Fig. 4a), in addition to Si, Al and K agrees with the presence of phlogopite, also detected
394 by XRD.

395 The sample SUMA5_1 (Fig. 2, Table 1), observed by backscattered electrons (BSE), consists of dark
396 grey grains (the abovementioned Si-Al-Ca matrix) on which brighter micrometric particles, mainly
397 constituted by heavy elements, are finely dispersed (Fig. 4b-d). EDS spectra indicate variable
398 proportions of Sb, O, Ca and Fe; matching the EDS semiquantitative analyses with the XRD on the
399 same samples (Table 1), the presence of Sb oxides (sénarmontite and valentinite), Sb-Ca oxides and
400 schafarzikite can be assessed. The mopungite is recognizable as pale grey encrustation.

301 Before SEM analysis, the sample SS7 was treated in order to analyse separately the powder forming
302 a patina of alteration and the underlying surface (Fig. 2). For this purpose, the powder was gently
303 withdrawn with a spatula then the sample was immersed in ultrapure water (Millipore, Milli-Q[®], 18.2
304 MΩ cm⁻¹) for 20 minutes and successively washed with ultrapure water. The EDS spectra of both
305 powder and washed SS7 samples show an elemental composition of the matrix compatible with the
306 presence of NaAl-silicate hydrate and calcite in agreement with mineralogical results (Fig. 4e-g). Iron
307 is widely detected in both powder and washed samples, maybe due to its presence as impurities or as
308 rare crystallographic disordered phases not revealed by XRD analysis. BSE images of washed sample
309 highlight numerous fractures and holes of dissolution on the surface, reasonably linked to alteration
310 processes (Fig. 4g). These discontinuities are often filled up by microcrystals of Sb-oxides and
311 mopungite that rarely show a proper habitus, while in the dissolution cavity euhedral crystals of
312 mopungite (~ 100 μm) are well visible (Figs. 4h and i).

313 A semi-quantitative estimate based on EDS analysis performed on several samples, indicates variable
314 proportions of Na and Sb for the mopungite, which can be attributable to the different local
315 availability of Na and to different precipitation/crystallization conditions.

316 BSE image of casting residue SS5, sampled in the Riu Su Suergiu riverbank, shows dark flakes with
317 lamellar structures covered by euhedral grains likely bearing heavier elements (more pale grey) (Fig.
318 5a). The EDS spectra (Figs. 5b and c) indicate the presence of Sb, mainly concentrated in the pale
319 grey grains, in addition to Na, Al, Si e O and minor amounts of Fe and Zn, suggesting that the sample
320 is composed by a matrix of silicates with minor Sb phases. These findings agree with XRD patterns
321 indicating the presence of quartz and high-temperature silicates derived from metallurgical processes
322 (mullite, moissanite and cristobalite) and, subordinately, Sb-bearing phases. In this case, mopungite
323 was not detected, neither by XRD nor by SEM analyses.

324 Differently from the other types of metallurgical residues, the sample MET has a shiny surface (Fig.
325 2): the XRD patterns indicate that the sample is almost completely composed by metallic Sb with
326 minor amounts of quartz and other silicates (Fig. S1). BSE imaging shows a light grey surface made
327 up by compactly packed lamellae, in direct contact with a porous and irregular surface consisting of
328 aggregates of euhedral crystals (Fig. 5d). Results of EDS analysis indicate that the lamellar part is
329 mainly composed of metallic Sb whereas the porous zone, consisting of Sb oxide, represents an
330 oxidation surface (Figs. 5e and f). Traces of Si, Al, Na, Ca, K and O, likely due to the presence of
331 silicates, were observed in EDS spectra (not shown).

332 Quantitative chemical analyses were performed by EMP on samples selected after SEM observation.
333 The results are reported in Tables 3, 4 and 5 showing the composition of metallic Sb, mopungite-like
334 phases and Na-Ca silicates, respectively. The exact position of the spot analyses is shown in figures

335 S4 and S5. EMP analyses confirm the reliability of the results obtained by XRD and SEM
336 investigations.

337 Metallic Sb is almost pure with small amounts of Sn (0.41-0.46 wt.%): it has been found in the
338 samples MET as well as in SS7 and SUMA-5_4, as small droplets. The sample MET hosts also small
339 inclusions of a Sb-Fe alloy with a ratio of about 80:20 and Sb oxides as surficial encrustations (Table
340 3, Fig. S4). Among the Sb oxides, both Sb_2O_3 and Sb_2O_4 were identified by calculating the
341 stoichiometric oxygen required to fulfil the cations amount, up to reach approximately 100 wt.% ox.
342 This finding supports the XRD analyses that detected senarmontite, valentinite and schafarzikite.

343 Several spot analyses were performed on mopungite crystals found by SEM-EDS investigation in
344 three samples of foundry slags (SUMA_5_4, SS7, SUMA_5_1). As already observed by EDS spectra,
345 the relative proportions of Sb and Na vary from one crystal to another with Sb_2O_5 ranging 70.44-
346 79.55 wt.% and Na_2O 7.64-10.84 wt.%. Minor amounts of other oxides, especially SiO_2 (0.25-1.62
347 wt.%) and FeO , Sn_2O , ZnO , Al_2O_3 (< 1 wt.%) were also detected (Table 4, Fig. S5). Interestingly,
348 none of the dozens analysed points have a composition closely matching that of an ideal mopungite
349 that, according to its stoichiometry, should be 65.54 wt.% Sb_2O_5 , 12.56 wt.% Na_2O and 21.90 wt.%
350 H_2O . Indeed, all points are more or less enriched in Sb and deficient in Na and have a water content
351 (estimated as the difference between the ideal oxides sum of 100 wt.% and the measured one of about
352 80-90 wt.%) lower than expected (see discussion below).

353 Further analyses were performed on the silicate phases in the attempt to characterize the complex
354 matrix of the slags (Table 5, Figs. S4-5). The identification of several phases is complicated by their
355 low total cations sums, likely due to the presence of hydroxyl and/or carbonate and/or sulphate
356 groups. For instance, the Na-rich alumino-silicates are recognized as cancrisilite or kyanoxalite
357 (cancrinite group) based on the contents of the main cations and by the oxides sum (about 90 wt.%)
358 compatible with the presence of about 10 wt.% of $H_2O + CO_2$. Likewise, Ca-silicates have been
359 identified as spurrite or hillebrandite, both characterized by approximately 30 wt.% SiO_2 and 60 wt.%
360 CaO , and with about 10 wt.% CO_2 and H_2O , respectively. Many other analytical spots provided
361 chemical compositions with variable contents of SiO_2 , Al_2O_3 , CaO and Na_2O and with low oxides
362 sums, but a clear match with known minerals could not be established. However, by comparing EMP
363 analyses with the XRD mineral identification, some further constraints on slags mineralogy can be
364 provided. For instance, minerals like nosean and hauyne were not precisely identified by EMP but
365 their presence is reliably inferred by some spot analyses, showing compositions close to these phases,
366 and by their finding through XRD.

367 Quartz, calcite, dolomite and gypsum were detected by EDS spectra but not analysed by WDS.
368 Although recognized by XRD analyses, no phyllosilicates were found by EMP likely due to the

369 different sample preparation required by the two techniques. Indeed, grinding the whole sample for
370 XRD analyses allow to include its external surface, whereas cutting and polishing the slabs for EMP
371 analyses imply the loss of the external surface where phyllosilicates are likely concentrated as
372 alteration patinas.

373
374
375

5. Discussion

376
377
378

5.1 Case study

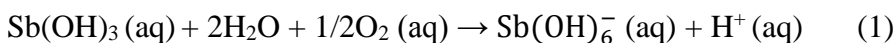
379
380
381

The ore minerals hosted in the mine waste (and subordinately in the natural outcrops) and the Sb-
bearing phases in the foundry slag heaps represent the main sources of Sb from Su Suergiu area. The
mineralogical associations, detected by XRD analysis, suggest that Sb is released through i) oxidation
of primary Sb sulphides (in mine wastes and natural outcrops) and ii) weathering of Sb-bearing phases
dumped in the foundry slag heaps (Fig. 6).

382
383
384

Previous authors (Ashley et al., 2003) indicated two main pathways of stibnite oxidation in contact
with circumneutral waters under oxidizing conditions: the direct oxidative dissolution and the
formation of Sb(III)-oxides which successively dissolve. In both cases, Sb(III) is released in solution
where is present as dissolved Sb(OH)₃. Under oxidizing conditions and near-neutral pH values,
typical geochemical conditions of surface waters, Sb(OH)₃ is oxidized to Sb(OH)₆⁻ (Eq.1) (Oorts et
al., 2008) that is stable in solution and can be transported for a long distance downstream from the
contamination source.

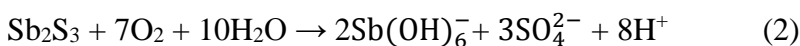
385
386
387



388
389
390

At Su Suergiu, the presence of gypsum in mine wastes (and outcropping rocks) indicates sulphide
oxidation due to exposition to surface environment. The mineralogical association linked to the
stibnite oxidation (Ashley et al., 2003) is not observed, suggesting the occurrence of direct oxidative
dissolution, as simplified in Eq. 2 (Cidu et al., 2018):

391
392
393



394
395
396

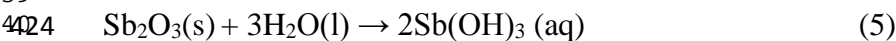
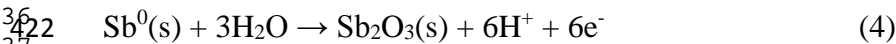
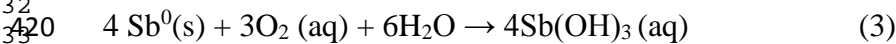
The dissolution of sulphides (not only stibnite, but also pyrite, arsenopyrite, etc.) is also proved by
the high concentration of SO₄²⁻ (Cidu et al., 2021, 2018, 2014) in the water draining the mine area
(up to 1900 mg L⁻¹). Carbonates present in both natural outcrops and in the gangue (Table 1),
neutralize the acidity of solutions to circumneutral - slightly alkaline pH, promoting further oxidation

397
398
399
400
401
402
403
404
405

402 and Sb mobilization.

403 The high Sb concentration, up to 30,000 µg/L Sb in waters draining the Su Suergiu mine area,
404 indicates the foundry slag heaps as the main source of Sb released in the environment (Cidu et al.,
405 2021, 2018, 2014). This finding agrees with data reported by Contini et al. (2009) showing mean
406 value of 1% Sb in solid samples collected along the Rio Su Suergiu and Rio Sessini, and dramatically
407 higher Sb content, from few unit % up to about 17 wt% Sb in samples collected in the foundry slag
408 heaps. The high variability observed within the foundry slag heaps, is probably due to the
409 inhomogeneity of the foundry products dumped there. This is supported by the abundance and
410 variability of Sb mineralogical phases observed in foundry slag samples in our study (Table 1, Fig.
411 S1).

412 The mineralogical associations observed in different foundry slag samples suggest complex alteration
413 schemes, whose simplified examples are reported in figure 6. The metallic Sb and Sb-oxides are
414 recognized as the primary minerals of Sb contamination, however Fe-Sb alloy and tetrahedrite are
415 also rarely detected. The primary metallic Sb can be dissolved to Sb(OH)₃ (Eq. 3) (Ilgen et al., 2014)
416 or oxidized to valentinite (Eq. 4) (Lide 2005, modified). The valentinite can dissolve and release
417 Sb(OH)₃(aq) (Eq. 5) (Biver & Shotyk, 2013; Oorts et al., 2008), or be further oxidized to cervantite
418 that successively releases Sb(OH)₃ (and presumably Sb(OH)₆) by dissolution.



425
426 In the same way, primary s enarmontite/ valentinite can follow the direct dissolution or the oxidation
427 to cervantite. Once in solution, the Sb(OH)₃, at oxidizing conditions and slightly alkaline pH of
428 draining water (7.1 < pH < 8.5) (Cidu et al., 2021, 2018, 2015), quickly oxidize to Sb(OH)₆⁻ (Eq.1).

429 The mopungite is the last-forming mineral of the proposed weathering schemes. The abundant
430 presence of this mineral is the peculiarity of the studied system, in fact mopungite has been reported
431 only in seven locations around the world (data from www.mindat.org/show.php?id=2777&ld=1),
432 because it forms in presence of high concentrations of Sb(OH)₆⁻ and Na⁺ (> 20 mM) (Blandamer et
433 al., 1974; Ilgen et al., 2014).

434 Figure 7a displays an Eh-pH diagram of Sb for the system Na-Sb-S-H-O, built by using the
435 composition of the slag drainage sample SU2 (30.10.2012) (Fig.2) from Cidu et al. (2014). According

436 to thermodynamic equilibrium conditions, despite the high Sb ($30,000 \mu\text{g L}^{-1}$, i.e. 0.25 mM) and Na
437 (600 mg L^{-1} , i.e. 26.10 mM) concentrations, mopungite precipitation is not predicted at the oxidizing
438 conditions characterizing drainages from the investigated area (red circle), while the $\text{Sb}(\text{OH})_6^-$ species
439 is stable in solution (Filella et al. 2002). In agreement, mopungite was not detected in the XRD
440 patterns of samples collected downstream the foundry slag heaps. Apparent mopungite formation was
441 found by increasing either 1.7 times the Na concentrations (Fig. 7b) or 1.8 times that of Sb (Fig. 7c).
442 These findings suggest that the apparent formation of mopungite is related to local water chemistry
443 and cannot be predicted based on bulk water chemistry downstream to foundry slags. The favourable
444 conditions for precipitation can likely be reached during drying of foundry wastes that lead to local
445 and variable Na and Sb concentrations.

446 In the foundry slag heaps of Su Suergiu, the abundance of Na phases derived from metallurgical
447 processes explains the enrichment of Na^+ in solution and allows the mopungite precipitation, that
448 limit the Sb dispersion by bonding $\text{Sb}(\text{OH})_6^-$. SEM imaging (Fig. 4) shows that mopungite can
449 precipitate as euhedral crystals, as microcrystal in veinlets within the NaAl-silicates hydrate matrix
450 and as encrustation on altered surfaces of grains. This variability can be due to local differences of
451 geochemical and kinetic conditions at the microscale. For example, in the dissolution cavities the
452 precipitation of euhedral crystals might be promoted by the stagnation of concentrated solution. The
453 velocity of circulation/percolation of solutions within the foundry slag heaps can influence the local
454 concentration (linked to the contact time solid/solution) and the migration of the elements leading to
455 the precipitation of secondary minerals with different composition and crystallinity, as supported by
456 the variability of relative proportion of Na and Sb detected by WDS analyses. The common Na
457 deficiency observed in mopungite-like phases suggests that the Na availability in the slag matrix is
458 the limiting factor in the mopungite formation. On the contrary, the high Sb contents in mopungite is
459 the result of the availability of this element in the slags, as testified by the widespread occurrence of
460 micro disseminations of metallic and oxidized Sb. The inconsistency between XRD refinement data,
461 indicating a perfect mopungite, and chemical analyses, pointing to a non-ideal phase, may depend on
462 the position of the analysed phases within the slag fragments. XRD analyses were performed on
463 powder grasped from the surface of slag fragments whereas EMP analyses, requiring the samples cut
464 into polished slabs, were unavoidably performed on crystals intersected in the inner part of the
465 samples. This difference in mopungite composition can shade a light on its formation mechanism.
466 Antimony released in solution from the Sb droplets reacts with Na-rich silicates in the surrounding
467 matrix resulting in the formation of mopungite-like phases. The Na enrichment increases as fluids
468 migrate toward the surface of the slags where alternating dry-wet cycles, due to the weather
469 conditions, enhance the precipitation of a “real” mopungite.

470 Metallic Sb is far from equilibrium conditions (Fig. 7, red circle), and it is probably easily oxidized
471 or dissolved in the investigated system, representing a considerable source of Sb. In agreement with
472 the thermodynamic prediction, we identified Sb oxidation surfaces on metallic Sb in MET sample by
473 EDS-SEM analysis (Fig. 5d-f).

474 The stibnite field extends from acidic to alkaline conditions (pH 8.7) at anoxic conditions, but an
475 increase in Eh values can lead to the formation of Sb oxides or to a direct dissolution. As stated above,
476 the direct oxidative dissolution (*sensu* Ashley et al., 2003) seems to be the prevalent process at Su
477 Suergiu, since the mineralogical association linked to the stibnite oxidation was not found.

478 The abundance of mopungite observed through both XRD and SEM analyses indicates that it is the
479 main trap of dissolved $\text{Sb}(\text{OH})_6^-$ for which represent a (temporary) sink in function of the change of
480 geochemical and hydrological conditions. In fact, it must be considered that under high flow
481 condition, the dilution can lead to the mopungite dissolution and thus to the re-mobilization of Sb.
482 This could explain the high Sb concentrations in waters reported by Cidu et al. (2014, 2018) after
483 storm events, despite the dilution linked to the consistent increase of water flow. The role of metal
484 oxy-hydroxides in limiting the Sb mobility, often reported in literature (Beauchemin et al., 2012;
485 Craw et al., 2004; Ilgen et al., 2014; Ritchie et al., 2013; Wilson et al., 2004), does not seem to be
486 very effective at Su Suergiu; indeed, the rare occurrence of phases like FeSb-ox and CaSb-ox can just
487 subordinately contribute to Sb immobilization due the local availability of metals.

489 5.2 Broader implications

490 The role of secondary Sb minerals on Sb mobility in supergene and anthropic environments is
491 examined in several studies and can be useful to understand the apparently ambiguous behaviour of
492 Sb. As highlighted by Majzlan et al. (2016), mineralogical studies consider Sb as a low mobile
493 element since it tends to form poorly soluble phases such as tripuhyte (FeSbO_4), while many
494 geochemical studies report a high Sb mobility inferred by its high concentrations in the surrounding
495 waters. The key to understand such a contrasting behaviour is to consider the role of secondary phases,
496 especially their stability in specific environmental conditions, the oxidation pathways and the
497 conditions limiting or enhancing their crystallization, and the kinetics of formation/dissolution
498 reactions. As an instance, some secondary minerals can bind Sb only in specific conditions, thus they
499 do not have relevance in the Sb retention where these conditions are not fulfilled (Roper et al., 2015).
500 Several papers document that Sb released in the environment, due to oxidation of stibnite and other
501 Sb-bearing minerals, can be adsorbed onto metal oxy/hydroxides (Fe, Mn, Al) or co-precipitated with
502 secondary minerals (Beauchemin et al., 2012; Craw et al., 2004; Ilgen et al., 2014; Ritchie et al.,

503 2013; Wilson et al., 2004) thus contributing to natural attenuation of $\text{Sb}(\text{OH})_6^-$. Also jarosite, by
504 means of the substitution of Fe with Sb, appears to be efficient for Sb immobilization (Courtin-
505 Nomade et al., 2012). In tailings enriched in Fe compounds, the immobilization of Sb by means of
506 adsorption or coprecipitation with Fe phases, results more effective and stable than the precipitation
507 of Sb secondary minerals (Ashley et al., 2003; Borčinová Radková et al., 2020).
508 The role of mopungite in Sb mobility at Su Suergiu mine seems to be a peculiar case study since
509 mopungite has been found in few localities worldwide. On the contrary, it could be a process more
510 common than expected since alkali, especially Na-compounds, are largely used in Sb smelting
511 processes, resulting in the production of huge amounts of hazardous wastes called alkali residues
512 (Guo et al., 2014; Long et al., 2020; Su et al., 2021). These wastes are a source of contamination and
513 are currently studied with the aim to estimate the potential release of toxic compounds (Guo et al.,
514 2014), to reduce the environmental impact (Salihoglu, 2014), but also to recovery Sb, As, and sodium
515 bicarbonate to be reused in smelting processes (Long et al., 2020; Su et al., 2021). Thus,
516 understanding the processes affecting the Sb fate in Na-rich residues of metallurgical plants is a
517 current and worldwide concern.

518
519

519 **6. Conclusions**

520 In this study, the peculiar conditions allowing the mopungite formation at Su Suergiu are described,
521 providing a new insight on its role on Sb mobility. At Su Suergiu, mopungite precipitation is due to
522 alteration of the natural thermodynamic equilibria induced by past mine and metallurgical activity,
523 and it acts as temporary sink for Sb contributing to reduce Sb dispersion in solution. The high Na
524 availability to solution in Su Suergiu slags favours mopungite formation. These findings are
525 fundamental to understand the mineralogical and geochemical processes occurring in the investigated
526 area, and they shed light on the mechanisms responsible for Sb mobility, representing a fundamental
527 tool to plan future remediation actions at Su Suergiu and elsewhere.

528
529

529 **Declaration of competing interest**

530 The authors declare that they have no known competing financial interests or personal relationships
531 that could have appeared to influence the work reported in this paper.

532
533

533 **Acknowledgement**

534 The authors acknowledge PRIN 2017 MINERAL REACTIVITY, A KEY TO UNDERSTAND

535
536
537
538
539
540
541
542
543
544
545

535 LARGE-SCALE PROCESSES: FROM ROCK FORMING ENVIRONMENTS TO SOLID WASTE
536 RECOVERING/LITHIFICATION, CESA (E58C16000080003) from RAS and RAS/FdS
537 (F72F16003080002) grants, and the CeSAR (Centro Servizi d'Ateneo per la Ricerca) of the
538 University of Cagliari, Italy, for SEM analysis. This work has been supported by the POR FESR
539 Sardegna 2014–2020 (project cluster Top-Down: TESTARE). Special thanks to many students for
540 their support in the samples collecting and analysis. We acknowledge the financial support for the
541 synchrotron radiation XRD approved at MCX-ELETTRA beamline, and the MCX beamline staff for
542 the technical support in the management of the beamline. CM acknowledge the support by the Grant
543 to Department of Science, Roma Tre University (MIUR-323 Italy Departments of Excellence, Article
544 1, Comma 314–337, Law 232/2016).

545

546 **References**

547

547 Álvarez-Ayuso, E., Otones, V., Murciego, A., García-Sánchez, A., & Regina, I. S. (2013). Mobility and
548 phytoavailability of antimony in an area impacted by a former stibnite mine exploitation. *Science of the*
549 *Total Environment*, 449, 260–268. <https://doi.org/10.1016/j.scitotenv.2013.01.071>

550

550 Amat di San Filippo, P. (2014). *L'Antimonio in Sardegna e la Fonderia di Villasalto*.

551

551 Asai, T. (1975). Refinement of the Crystal Structure of Sodium Hexahydroxoantimonate(V), NaSb(OH)₆.
552 *Bulletin of the Chemical Society of Japan*, 48(10), 2677–2679. <https://doi.org/10.1246/bcsj.48.2677>

553

553 Ashley, P. M., Craw, D., Graham, B. P., & Chappell, D. A. (2003). Environmental mobility of antimony around
554 mesothermal stibnite deposits, New South Wales, Australia and southern New Zealand. *Journal of*
555 *Geochemical Exploration*, 77(1), 1–14. [https://doi.org/10.1016/S0375-6742\(02\)00251-0](https://doi.org/10.1016/S0375-6742(02)00251-0)

556

556 Ashley, P. M., Craw, D., Tighe, M. K., & Wilson, N. J. (2006). Magnitudes, spatial scales and processes of
557 environmental antimony mobility from orogenic gold-antimony mineral deposits, Australasia.
558 *Environmental Geology*, 51(4), 499–507. <https://doi.org/10.1007/s00254-006-0346-6>

559

559 Bagherifam, S., Brown, T. C., Wijayawardena, A., & Naidu, R. (2021). The influence of different antimony
560 (Sb) compounds and ageing on bioavailability and fractionation of antimony in two dissimilar soils.
561 *Environmental Pollution*, 270, 116270. <https://doi.org/10.1016/j.envpol.2020.116270>

562

562 Beauchemin, S., Kwong, Y. T. J., Desbarats, A. J., MacKinnon, T., Percival, J. B., Parsons, M. B., & Pandya,
563 K. (2012). Downstream changes in antimony and arsenic speciation in sediments at a mesothermal gold
564 deposit in British Columbia, Canada. *Applied Geochemistry*, 27(10), 1953–1965.
565 <https://doi.org/10.1016/j.apgeochem.2012.04.003>

566

566 Bittarello, E., Cámara, F., Ciriotti, M. E., & Marengo, A. (2015). Ottensite, brizziite and mopungite from Pereta

567

568

569

570

571

- 567 mine (Tuscany, Italy): new occurrences and crystal structure refinement of mopungite. *Mineralogy and*
568 *Petrology*, 109(4), 431–442. <https://doi.org/10.1007/s00710-015-0375-5>
569 Biver, M., & Shotyk, W. (2013). Stibiconite (Sb₃O₆OH), senarmontite (Sb₂O₃) and valentinite (Sb₂O₃):
570 Dissolution rates at pH 2–11 and isoelectric points. *Geochimica et Cosmochimica Acta*, 109, 268–279.
571 <https://doi.org/10.1016/j.gca.2013.01.033>
572 Blandamer, M. J., Burgess, J., & Peacock, R. D. (1974). Solubility of sodium hexahydroxoantimonate in water
573 and in mixed aqueous solvents. *Journal of the Chemical Society, Dalton Transactions*, 10, 1084–1086.
574 <https://doi.org/10.1039/DT9740001084>
575 Borčinová Radková, A., Jamieson, H. E., & Campbell, K. M. (2020). Antimony mobility during the early
576 stages of stibnite weathering in tailings at the Beaver Brook Sb deposit, Newfoundland. *Applied*
577 *Geochemistry*, 115, 104528. <https://doi.org/10.1016/j.apgeochem.2020.104528>
578 Borčinová Radková, A., Jamieson, H. E., Campbell, K. M., & Hudson-Edwards, K. A. (2022). Antimony in
579 Mine Wastes: Geochemistry, Mineralogy, and Microbiology. *Economic Geology*.
580 <https://doi.org/10.5382/econgeo.4937>
581 Carmignani, L., Conti, P., Barca, S., Cerbai, N., Eltrudis, A., Funedda, A., Oggiano, G., Patta, E. D., Ulzega,
582 A., & Orrù, P. (2001). Note illustrative della Carta Geologica d'Italia Foglio 549 “Muravera”, alla scala
583 1:50.000. Servizio Geologico d'Italia. *Regione Autonoma Della Sardegna, Italy*, 140.
584 Carmignani, L., Cortecci, G., Dessau, G., Duchi, G., Oggiano, G., Pertusati, P., & Saitta, M. (1978). The
585 Antimony and Tungsten Deposit of Villasalto in South-Eastern Sardinia and its Relationship with
586 Hercynian Tectonics. *Schweiz. Mineral. Petrogr. Mitt.*, 58, 163–188. <https://doi.org/10.5169/seals-45197>
587 Cidu, R., Biddau, R., & Dore, E. (2015). Determination of traces of Sb(III) using ASV in Sb-rich water samples
588 affected by mining. *Analytica Chimica Acta*, 854, 34–39. <https://doi.org/10.1016/j.aca.2014.11.020>
589 Cidu, R., Biddau, R., Dore, E., Vacca, A., & Marini, L. (2014). Antimony in the soil–water–plant system at
590 the Su Suergiu abandoned mine (Sardinia, Italy): Strategies to mitigate contamination. *Science of The*
591 *Total Environment*, 497–498, 319–331. <https://doi.org/10.1016/j.scitotenv.2014.07.117>
592 Cidu, R., Biddau, R., Frau, F., Wanty, R. B., & Naitza, S. (2021). Regional occurrence of aqueous tungsten
593 and relations with antimony, arsenic and molybdenum concentrations (Sardinia, Italy). *Journal of*
594 *Geochemical Exploration*, 229, 106846. <https://doi.org/10.1016/j.gexplo.2021.106846>
595 Cidu, R., Dore, E., Biddau, R., & Nordstrom, D. K. (2018). Fate of Antimony and Arsenic in Contaminated
596 Waters at the Abandoned Su Suergiu Mine (Sardinia, Italy) . *Mine Water and the Environment*, 37(1),
597 151–165. <https://doi.org/10.1007/s10230-017-0479-8>

- 598 Contini, E., Naitza, S., Tocco, S., Garau, A., Buosi, M., & Sarritzu, R. (2009). Fenomeni di contaminazione
599 da discariche minerarie e metallurgiche nel Distretto dell'Antimonio del Sarrabus-Gerrei (Sardegna Sud-
600 Orientale): l'area di Su Suergiu-Villasalto. *Resoconti Dell'Associazione Mineraria Sarda*, 112–113, 45–
601 83.
- 602 Courtin-Nomade, A., Rakotoarisoa, O., Bril, H., Grybos, M., Forestier, L., Foucher, F., & Kunz, M. (2012).
603 Weathering of Sb-rich mining and smelting residues: Insight in solid speciation and soil bacteria toxicity.
604 *Chemie Der Erde*, 72(4), 29–39. <https://doi.org/10.1016/j.chemer.2012.02.004>
- 605 Craw, D., Wilson, N., & Ashley, P. M. (2004). Geochemical controls on the environmental mobility of Sb and
606 As at mesothermal antimony and gold deposits. *Applied Earth Science*, 113(1), 3–10.
607 <https://doi.org/10.1179/037174504225004538>
- 608 Diemar, G., Filella, M., Leverett, P., & Williams, P. (2009). Dispersion of antimony from oxidizing ore
609 deposits. *Pure and Applied Chemistry*, 81, 1547–1553. <https://doi.org/10.1351/PAC-CON-08-10-21>
- 610 European Commission. (1998). *Official Journal of the European Communities, COUNCIL DIRECTIVE*
611 *98/83/EC*.
- 612 Filella, M. (2011). Antimony interactions with heterogeneous complexants in waters, sediments and soils: A
613 review of data obtained in bulk samples. *Earth-Science Reviews*, 107(3–4), 325–341.
614 <https://doi.org/10.1016/j.earscirev.2011.04.002>
- 615 Filella, M., Belzile, N., & Chen, Y.-W. (2002a). Antimony in the environment: a review focused on natural
616 waters: II. Relevant solution chemistry. *Earth-Science Reviews*, 59(1), 265–285.
617 [https://doi.org/https://doi.org/10.1016/S0012-8252\(02\)00089-2](https://doi.org/https://doi.org/10.1016/S0012-8252(02)00089-2)
- 618 Filella, M., Belzile, N., & Chen, Y.-W. (2002b). Antimony in the environment: A review focused on natural
619 waters I. Occurrence. *Earth-Science Reviews*, 57, 125–176. [https://doi.org/10.1016/S0012-8252\(01\)00070-8](https://doi.org/10.1016/S0012-8252(01)00070-8)
- 620
621 Filella, M., Williams, P. A., & Belzile, N. (2009). Antimony in the environment: knowns and unknowns.
622 *Environmental Chemistry*, 6(2), 95–105. <https://doi.org/10.1071/EN09007>
- 623 Fowler, B. A., & Goering, P. L. (1991). Antimony. In E. Merian (Ed.), *Metals and Their Compounds in the*
624 *Environment* (pp. 743–750). Verlagsgesellschaft, Weinheim.
- 625 Friedrich, A., Wildner, M., Tillmanns, E., & Merz, P. L. (2000). Crystal chemistry of the new mineral
626 brandholzite, $Mg(H_2O)_6 [Sb(OH)_6]_2$, and of the synthetic analogues $M^{2+} (H_2O)_6 [Sb(OH)_6]_2$ ($M^{2+} =$
627 Mg, Co). *American Mineralogist*, 85(4), 593–599. <https://doi.org/10.2138/am-2000-0422>
- 628 Funedda, A., Naitza, S., Buttau, C., Cocco, F., & Dini, A. (2018). Structural controls of ore mineralization in

- 629 a polydeformed basement: field examples from the variscan bacca locci shear zone (SE Sardinia, Italy).
630 *Minerals*, 8(10), 23. <https://doi.org/10.3390/min8100456>
631 Funedda, A., Naitza, S., & Tocco, S. (2005). *Caratteri giacimentologici e controlli strutturali nelle*
632 *mineralizzazioni idrotermali tardo-erciniche ad As-Sb-W-Au del basamento metamorfico paleozoico*
633 *della Sardegna sud-orientale. Resoconti Associazione Mineraria Sarda* 110. 25–46.
634 Gebel, T. (1997). Arsenic and antimony: Comparative approach on mechanistic toxicology. *Chemico-*
635 *Biological Interactions*, 107(3), 131–144. [https://doi.org/10.1016/S0009-2797\(97\)00087-2](https://doi.org/10.1016/S0009-2797(97)00087-2)
636 Gurnani, N., Sharma, A., & Talukder, G. (1994). Effects of antimony on cellular systems in animals - A review.
637 *Nucleus*, 37, 71–96.
638 Hayes, W. J. J., & Jr., L. E. R. (Eds.). (1991). Volume 3, Classes of Pesticides. In *Handbook of Pesticide*
639 *Toxicology* (p. 1527). Academic Press, Inc.
640 He, M., Wang, N., Long, X., Zhang, C., Ma, C., Zhong, Q., Wang, A., Wang, Y., Pervaiz, A., & Shan, J.
641 (2019). Antimony speciation in the environment: Recent advances in understanding the biogeochemical
642 processes and ecological effects. *Journal of Environmental Sciences*, 75, 14–39.
643 <https://doi.org/10.1016/j.jes.2018.05.023>
644 IGEA, S. p. A. (2009). *Piano di investigazione iniziale dell'area mineraria di "Su Suergiu". Campo Pisano.*
645 Ilgen, A. G., Majs, F., Barker, A. J., Douglas, T. A., & Trainor, T. P. (2014). Oxidation and mobilization of
646 metallic antimony in aqueous systems with simulated groundwater. *Geochimica et Cosmochimica Acta*,
647 132, 16–30. <https://doi.org/10.1016/j.gca.2014.01.019>
648 Johnson, C. A., Moench, H., Wersin, P., Kugler, P., & Wenger, C. (2005). Solubility of antimony and other
649 elements in samples taken from shooting ranges. *Journal of Environmental Quality*, 34(1), 248–254.
650 <https://doi.org/10.2134/jeq2005.0248>
651 Leverett, P., Reynolds, J. K., Roper, A. J., & Williams, P. A. (2012). Tripuhyite and schafarzikite: two of the
652 ultimate sinks for antimony in the natural environment. *Mineralogical Magazine*, 76(4), 891–902.
653 <https://doi.org/10.1180/minmag.2012.076.4.06>
654 Lide, D. R. (2005). *CRC Handbook of Chemistry and Physics*. CRC Press, Boca Raton, FL.
655 Majzlan, J., Lalinská, B., Chovan, M., Bläß, U., Brecht, B., Göttlicher, J., Steininger, R., Hug, K., Ziegler, S.,
656 & Gescher, J. (2011). A mineralogical, geochemical, and microbiological assessment of the antimony- and
657 arsenic-rich neutral mine drainage tailings near Pezinok, Slovakia. *American Mineralogist*, 96(1), 1–13.
658 <https://doi.org/10.2138/am.2011.3556>
659 Majzlan, J., Števko, M., & Lánčzos, T. (2016). Soluble secondary minerals of antimony in Pezinok and

- 660 Kremnica (Slovakia) and the question of mobility or immobility of antimony in mine waters.
661 *Environmental Chemistry*, 13(6), 927–935. <https://doi.org/10.1071/EN16013>
662
- 662 Marzoni Fecia Di Cossato, Y., Meacci, C., Orlandi, R., & Vezzalini, G. (1987). The second world occurrence
663 of mopungite from the Pereta Mine, Tuscany, Italy. *Atti Della Società Toscana Di Scienze Naturali*
664 *Residente in Pisa, Memorie, Processi Verbali, Serie A*, 94, 135–138.
665
- 665 Mitsunobu, S., Takahashi, Y., Sakai, Y., & Inumaru, K. (2009). Interaction of Synthetic Sulfate Green Rust
666 with Antimony(V). *Environmental Science & Technology*, 43(2), 318–323.
667 <https://doi.org/10.1021/es8026067>
668
- 668 Momma, K., & Izumi, F. (2011). *{it VESTA3}* for three-dimensional visualization of crystal, volumetric and
669 morphology data. *Journal of Applied Crystallography*, 44(6), 1272–1276.
670 <https://doi.org/10.1107/S0021889811038970>
671
- 671 Multani, R. S., Feldmann, T., & Demopoulos, G. P. (2016). Antimony in the metallurgical industry: A review
672 of its chemistry and environmental stabilization options. *Hydrometallurgy*, 164, 141–153.
673 <https://doi.org/10.1016/j.hydromet.2016.06.014>
674
- 674 Ngo, L. K., Price, H. L., Bennett, W. W., Teasdale, P. R., & Jolley, D. F. (2020). DGT and selective extractions
675 reveal differences in arsenic and antimony uptake by the white icicle radish (*Raphanus sativus*).
676 *Environmental Pollution*, 259, 113815. <https://doi.org/10.1016/j.envpol.2019.113815>
677
- 677 Okkenhaug, G., Grasshorn Gebhardt, K. A., Amstaetter, K., Lassen Bue, H., Herzel, H., Mariussen, E.,
678 RossebøAlmås, Å., Cornelissen, G., Breedveld, G. D., Rasmussen, G., & Mulder, J. (2016). Antimony
679 (Sb) and lead (Pb) in contaminated shooting range soils: Sb and Pb mobility and immobilization by iron
680 based sorbents, a field study. *Journal of Hazardous Materials*, 307, 336–343.
681 <https://doi.org/10.1016/j.jhazmat.2016.01.005>
682
- 682 Okkenhaug, G., Zhu, Y.-G., Luo, L., Lei, M., Li, X., & Mulder, J. (2011). Distribution, speciation and
683 availability of antimony (Sb) in soils and terrestrial plants from an active Sb mining area. *Environmental*
684 *Pollution*, 159(10), 2427–2434. <https://doi.org/10.1016/j.envpol.2011.06.028>
685
- 685 Oorts, K., Smolders, E., Degryse, F., Buekers, J., Gascó, G., Cornelis, G., & Mertens, J. (2008). Solubility and
686 toxicity of antimony trioxide (Sb₂O₃) in soil. *Environmental Science & Technology*, 42(12), 4378–4383.
687 <https://doi.org/10.1021/es703061t>
688
- 688 Palenik, R. C., Abboud, K. A., & Palenik, G. J. (2005). Bond valence sums and structural studies of antimony
689 complexes containing Sb bonded only to O ligands. *Inorganica Chimica Acta*, 358(4), 1034–1040.
690 <https://doi.org/https://doi.org/10.1016/j.ica.2004.11.013>
691
- 691 Piatak, N. M., & Ettler, V. (2021). *Metallurgical Slags: Environmental Geochemistry and Resource Potential*.

- 692 The Royal Society of Chemistry. <https://doi.org/10.1039/9781839164576>
1
- 693 Protano, G., & Riccobono, F. (1997). Environmental levels of antimony, arsenic and mercury in the Tafone
3 mining area (Southern Tuscany, Italy). *Atti Soc. Tosc. Sci. Nat., Mem.*, 104, 75–83.
694
5
- 695 Puigdomènech, I. (2010). *HYDRA-MEDUSA (Make Equilibrium Diagrams Using Sophisticated Algorithms).
6 Windows interface to the MS-DOS versions of INPUT, SED and PREDOM (FORTRAN programs
9 drawing chemical equilibrium diagrams) Vers. 6 December 2010. Royal Institute of Technology (KTH),.
1097*
11
- 698 RAS. (1998). *Regione Autonoma della Sardegna - Nuovo studio dell'idrologia superficiale della Sardegna.
12 Cagliari: Assessorato della Programmazione, Bilancio ed Assetto del Territorio, Ente Autonomo del
13 Flumendosa.*
1499
15
- 700 RAS. (2013). *Carta geologica di base della Sardegna in scala 1:25000*, [http://www.sardegnaeoportale.
17
18
19
2002 it/argomenti/cartageologica.html](http://www.sardegnaeoportale.it/argomenti/cartageologica.html). Accessed Oct. 2013.
21
- 703 Rebuffi, L., Plaisier, J. R., Abdellatief, M., Lausi, A., Scardi, & Paolo. (2014). Mcx: A synchrotron radiation
22
23 beamline for X-ray diffraction line profile analysis. *Zeitschrift Fur Anorganische Und Allgemeine
24
25 Chemie*, 640(15), 3100–3106. <https://doi.org/10.1002/zaac.201400163>
26
27
- 706 Ritchie, V. J., Ilgen, A. G., Mueller, S. H., Trainor, T. P., & Goldfarb, R. J. (2013). Mobility and chemical fate
28
29 of antimony and arsenic in historic mining environments of the Kantishna Hills district, Denali National
30
31 Park and Preserve, Alaska. *Chemical Geology*, 335, 172–188.
32
33
34
35 <https://doi.org/10.1016/j.chemgeo.2012.10.016>
- 710 Roper, A. J., Leverett, P., Murphy, T. D., & Williams, P. A. (2015). Stabilities of byströmite, $MgSb_2O_6$,
37
38 ordoñezite, $ZnSb_2O_6$ and rosiaite, $PbSb_2O_6$, and their possible roles in limiting antimony mobility in the
39
40 supergene zone. *Mineralogical Magazine*, 79(3), 537–544. [https://doi.org/DOI:
41
42
43
44 10.1180/minmag.2015.079.3.03](https://doi.org/DOI:10.1180/minmag.2015.079.3.03)
- 714 Roper, A. J., Leverett, P., Murphy, T. D., & Williams, P. A. (2018). The stability of the rare sodium antimonate,
45
46 brizziite, and its role in Sb mobility. *Mineralogical Magazine*, 82(1), 89–93.
47
48
49
50 <https://doi.org/10.1180/minmag.2017.081.023>
- 717 Roper, A. J., Williams, P. A., & Filella, M. (2012). Secondary antimony minerals: Phases that control the
51
52 dispersion of antimony in the supergene zone. *Geochemistry*, 72(4), 9–14.
53
54
55
56 <https://doi.org/10.1016/j.chemer.2012.01.005>
- 720 Schrewelius, N. (1937). Röntgenuntersuchung der Verbindungen $NaSb(OH)_6$, $NaSbF_6$, $NaSbO_3$, und
57
58 gleichartiger Stoffe. *Zeitschrift Fur Anorganische Und Allgemeine Chemie*, 223(1935), 241–254.
59
- 722 Secchi, F., & Lorrai, M. (2001). Some geological and environmental aspects of the Sàrrabus-Gerrei Region
60
61
62
63
64
65

723 (SE Sardinia, Italy). *Rend. Sem. Fac. Sc. Univ. Cagliari*, 71.
1
2
3 724 Sejkora, J., Ozdin, D., & Duda, R. (2010). The supergene mineral association with brandholzite from Pernek,
4 Male Karpaty Mountains, Slovak Republic. *Journal of Geosciences*, 55(2), 149–160.
5
6 725 <https://doi.org/10.3190/jgeosci.064>
7
8
9 726
10 727 Toby, B. H. (2006). R factors in Rietveld analysis: How good is good enough? *Powder Diffraction*, 21(1), 67–
11 70. <https://doi.org/10.1154/1.2179804>
12
13 728
14 729 Toby, B. H., & Von Dreele, R. B. (2013). *{it GSAS-II}*: the genesis of a modern open-source all purpose
15 crystallography software package. *Journal of Applied Crystallography*, 46(2), 544–549.
16 730 <https://doi.org/10.1107/S0021889813003531>
17
18 731
19 732 WHO. (2011). *Guidelines for Drinking-water Quality* (4th ed.).
20
21 733
22 734 Williams, S. A. (1985). Mopungite, a new mineral from Nevada. *Mineralogical Record*, 15(1), 73–74.
23
24 735
25 736 Wilson, N. J., Craw, D., & Hunter, K. (2004). Antimony distribution and environmental mobility at an historic
26 antimony smelter site, New Zealand. *Environmental Pollution*, 129(2), 257–266.
27 737 <https://doi.org/10.1016/j.envpol.2003.10.014>
28
29
30
31
32 738
33
34
35
36
37
38
39
40
41
42
43
44
45
46
47
48
49
50
51
52
53
54
55
56
57
58
59
60
61
62
63
64
65

739 **Figure Captions**

1
2
3 740 **Fig 1.** Location of the study area (a, b) and schematic geological map of the Gerrei mine district (c)
4
5 741 (RAS, 2013, modified).

6
7 742 **Fig. 2.** Photos of representative samples of different types of metallurgical residues sampled at the
8
9 743 foundry slag heaps and waste runoff in Su Suergiu, and location of water and solids sampling point.

10
11 744 **Fig. 3.** Photo of the selected foundry slag SUMA 5_6 (a); synchrotron XRD patterns, after Rietveld
12
13 745 refinement performed by GSAS-II, of patinas scraped from the surface (b, c); the unit cell of
14
15 746 mopungite obtained by VESTA 3 software (d).

16
17
18 747 **Fig. 4.** SEM analysis: BSE images of casting residues SUMA 5_7 (a) and SUMA 5_1 (b, c and d),
19
20 748 the superficial powder withdrawn from SS7 sample (e and f) and the SS7 washed surface (g) with the
21
22 749 detail of mopungite microcrystals in the dissolution cavities (h and i). The labels refer to the
23
24 750 composition determined through the EDS spectra.

25
26 751 **Fig. 5.** BSE image (a) and the EDS spectra (b and c) of the casting residue SS5 sampled along the
27
28 752 Riu Suergiu riverbank, and BSE image (d) of MET sample, metallic antimony, with the EDS spectra
29
30 753 (e and f).

31
32 754 **Fig. 6.** Schematic representation of different alteration schemes proposed for the different Sb
33
34 755 contamination sources at Su Suergiu mine area.

35
36
37 756 **Fig. 7.** Eh vs pH diagrams for Sb in the system Sb – Na – S – H – O built by the chemical-equilibrium-
38
39 757 diagram-tool Hydra-Medusa (Puigdomènech, 2010). The red circle represents the water sample SU2
40
41 758 (30.10.2012) from Cidu et al. (2014).

42
43 759
44
45
46 760
47
48
49 761

50
51
52
53
54
55
56
57
58
59
60
61
62
63
64
65

Table 1. Mineralogical phases recognized through XRD analysis in outcropping rock and efflorescences and patinas, mine waste heaps and foundry slag heaps samples collected at Su Suergiu abandoned mine area. (abbreviations: Ank= ankerite; Apy= arsenopyrite; Ar= aragonite; Cal= calcite; Ccn= cancrinite; Cer= cervantite; Crs= cristobalite; Cus= cuspidine; Dol= dolomite; Fds= feldspar (group); Gr= graphite; Gy= gypsum; Hal= halotrichite; Hyn= hauyne; Hm= hematite; Hx= hexahydrate; Jar= jarosite; Kal= kalinite; Kie= kieserite; MgFe= magnesioferrite; Mt= magnetite; Mois= moissanite; Mop= mopungite; Mul= mullite; Nj= natrojarosite; Nsn= nosean; Pbj= plumbojarosite; Phy= phyllosilicates; Py= pyrite; Qtz= quartz; Sb= metallic Sb; Sck= schafarzikite; Sen= senarmonite; Stbn= stibnite; Td= tetrahedrite; Val= valtinite).

samples	description	mineralogical phases
Outcropping rocks		
SUMA 1	1A - yellowish efflorescence	Sulphate hydrate (mainly Fe) Hal, Kal, Jar/Pbj, Hx
	1B - fine grained material blue-grey	Qtz, Gy, Nj, Phy ¹
SUMA 2	1C - brown massive	Qtz, Gy, Phy ² , Py, Cal
	white patina	Qtz, Phy ³ , Cal, Ar
SS11		Qtz, Cal, Phy ⁴
SS12		Qtz, Gy, Al-sulphate-hyd, Ca-Al-sil-hyd, Jar, Phy ⁵
SS13	patina on black schist	Qtz, Gy, Phy ⁶
SS14		Qtz, Cal, Gy, Phy ⁷
SS15		Qtz, Cal, Gy, Phy ⁸ , Py-Cpy
¹ = muscovite, clinocllore; ² = muscovite, clinocllore, illite; ³ = clinocllore, muscovite; ⁴ = biotite, illite, clinocllore, muscovite; ⁵ = illite, muscovite; ⁶ = illite, clinocllore; ⁷ = illite, muscovite, clinocllore; ⁸ = clinocllore-Fe, muscovite		
Mine Waste		
SUMA 3	dark grey consolidated fine grainsize clasts, with quartz vein	Qtz, Phy ¹ , Cal, Dol
SUMA 4	dark fine grainsize clasts	Qtz, Gy, Phy ²
SS1	consolidate dark-grey clasts	Stbn, Qtz, Cal, Hm, Dol(Fe)
SS10	poorly consolidated fine grain size dark grey wastes	Qtz, Gy, Phy ³
¹ = muscovite, clinocllore; ² = muscovite, clinocllore; ³ = illite, clinocllore		
Foundry slag heaps		
<i>Residues of rotary furnace</i>		
SUMA 5A	massive poorly consolidated grey-dark fine grain size materials (5A) covered by friable red alteration crust (5A_red)	(5A) Qtz, Mop, Cal, NaAl-CO ₃ , Phy ¹ , Td, metal-ox; (5A_red) Mop, Apy, Qtz, Phy ² and Fe compounds derived from alteration
SUMA 5_4A	yellowish-brown consolidated lags, slightly altered	(5_4A) Mop, Val, Sen, Qtz, NaAl-CO ₃ , Cal, Nsn, Phy Hyn, metal-ox
SUMA 5_4B		(5_4B) Mop, Sen, Sb, Sb ₂ Fe, Qtz
SUMA 5_5	dark-brown slag, with red-yellowish patina	Mop, NaAl-silicate hyd, CaSb-ox, Qtz, Cal, Phy ² , Mul, Apy
<i>Casting residues</i>		
SUMA 5_1	slight brown foliated shell	Mop, Val, Sen, CaSb-ox, NaAl-silicate hyd, Mt(?), Sck
SUMA 5_2	yellowish granular patina on casting residues	Mop, Qtz, Cal, metal-ox
SUMA 5_6	yellowish and red patinas onto highly altered casting residues	Mop
SUMA 5_7	grey nodule partially consolidated, slightly altered	Mop, Cal, Phy ³ , NaAl-silicate hyd, Apy, Na-Mg/Al sulphates, Ank, Cus(?)
SS7	yellowish altered casting residues	Mop, Cal, Cer, NaAl-silicate hyd, Kie (?)
SS8	massive casting residues, slightly covered by yellowish patina of alteration	Mop, Val, Sen, Sb-ox, Dol, NaCa-sul, Phy ⁴ , Ccn (?)
<i>Slags</i>		
SUMA 5_3	black massive glassy slag, with brown elements	disordered carbon, Qtz, high temperature SiO ₂
<i>Metallic Sb</i>		
SS9	foliated dark residue with yellowish patina (uncertain origin)	Sb, Qtz Mop, Mois, Ccn (?), Gr
¹ = muscovite, clinocllore; ² = clinocllore, phlogopite; ³ = clinocllore; ⁴ = illite-montmorillonite, vermiculite; ⁵ = muscovite		
Waste runoff		
SS2	vacuolar /glassy brown slag	Qtz, Gy, Phy(?)
SS3	glassy slag	Qtz, Gy, Crs
SS4	vacuolar slightly glassy foundry slag	Qtz, Dol, Crs, Sb-ox, Fds, Phy(?), Sck
SS5	dark fine grain size (casting residues)	Qtz, Mul, Crs, Mois, Sb, Val
SS6	massive casting residues, slightly altered	Sb-ox, NaCa-silicate, MgFe

Table 2. Results of Rietveld refinement on two monomineralic samples within the $P 4_2/n$ space group. Cell parameters, Caglioti parameters and refinement quality parameters are reported (in brackets the uncertainty of the last decimal number). The atomic coordinates, occupancy, Thermal parameter (U_{iso}) and Wyckoff positions are also listed for the sample SUMA_5_6B.

	a=b (Å)	c (Å)	V (Å³)	$\alpha= \beta= \gamma$	U	V	W	GoF	wR
SUMA_5_6A	8.0184(1)	7.8872(1)	507.117	90	40.956	3.129	3.078	1.34	13.537
SUMA_5_6B	8.0219(1)	7.8887(1)	507.643	90	52.196	-7.316	3.711	1.45	12.903
<i>Structural details of SUMA_5_6B sample</i>									
			x	y	z	Occ.	U_{iso}	Site	Sym.
1	Sb	Sb	0	0	0	1	0.008	4c	-1
2	Na	Na	0	0.5	0	1	0.013	4d	-1
3	O	O1	0.0590	0.2206	0.0981	1	0.013	8g	1
4	H	H1	0.0318	0.2352	0.1938	1	0.019	8g	1
5	O	O2	-0.0872	-0.0695	0.2215	1	0.013	8g	1
6	H	H2	-0.2012	-0.088	0.2252	1	0.020	8g	1
7	O	O3	0.2231	-0.0761	0.0707	1	0.012	8g	1
8	H	H3A	0.2342	-0.1967	0.0641	0.5	0.018	8g	1
9	H	H3B	0.2351	-0.0664	0.1906	0.5	0.018	8g	1

Table 3. Selected analyses of metallic Sb, Sb-Fe alloy, and Sb-oxides

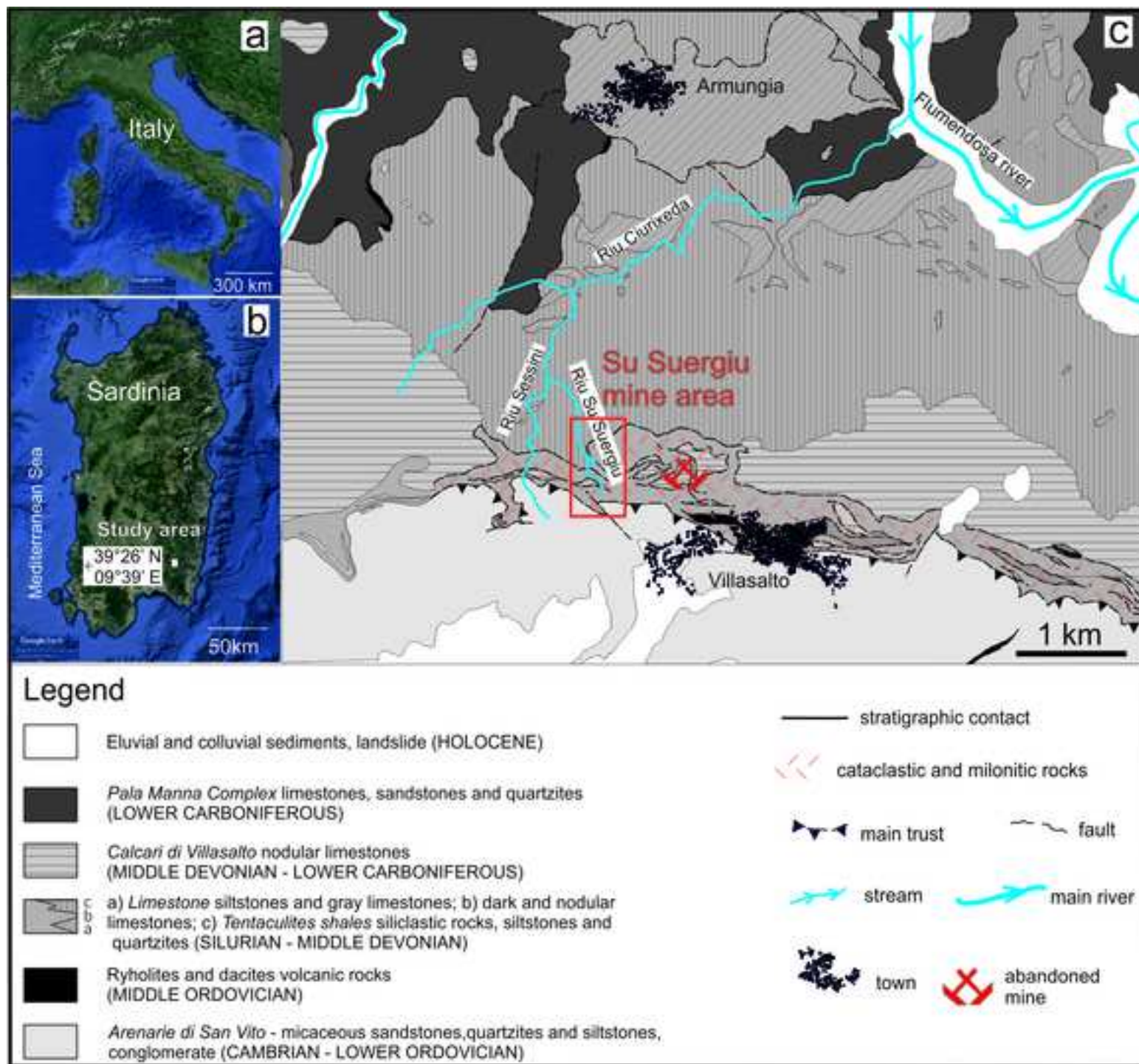
phase sample	Sb⁰				SbFe-alloy		Sb^{III}-ox			Sb^{III}Sb^V-ox	
	MET		SS7	SUMA-5_4	MET		Wt ox%	MET	SUMA-5_4	MET	SUMA-5_4
Wt el% / Point	1	2	7	8	3	5		6	9	4	10
Sb	100.09	99.99	100.72	99.20	79.10	80.02	Sb ₂ O ₃ *	98.4	98.53	99.06	87.07
Fe			0.08		20.18	20.09	FeO	0.11			0.21
Sn	0.41	0.46	0.43	0.42	0.29	0.33	SnO ₂	0.41	0.56	0.41	0.37
Zn				0.13			ZnO		0.2		0.2
Ni					0.41	0.13	NiO				
Co					0.11	0.15	CoO	0.085			
Mn				0.07			MnO				0.1
Si						0.03	SiO ₂	0.094	0.16	0.98	2.82
Ca							CaO				3.01
Na	0.04	0.04	0.06	0.10			Na ₂ O	0.1	0.13	0.19	5.11
Tot	100.54	100.49	101.29	99.92	100.09	100.76	Tot	99.2	99.59	100.63	98.89

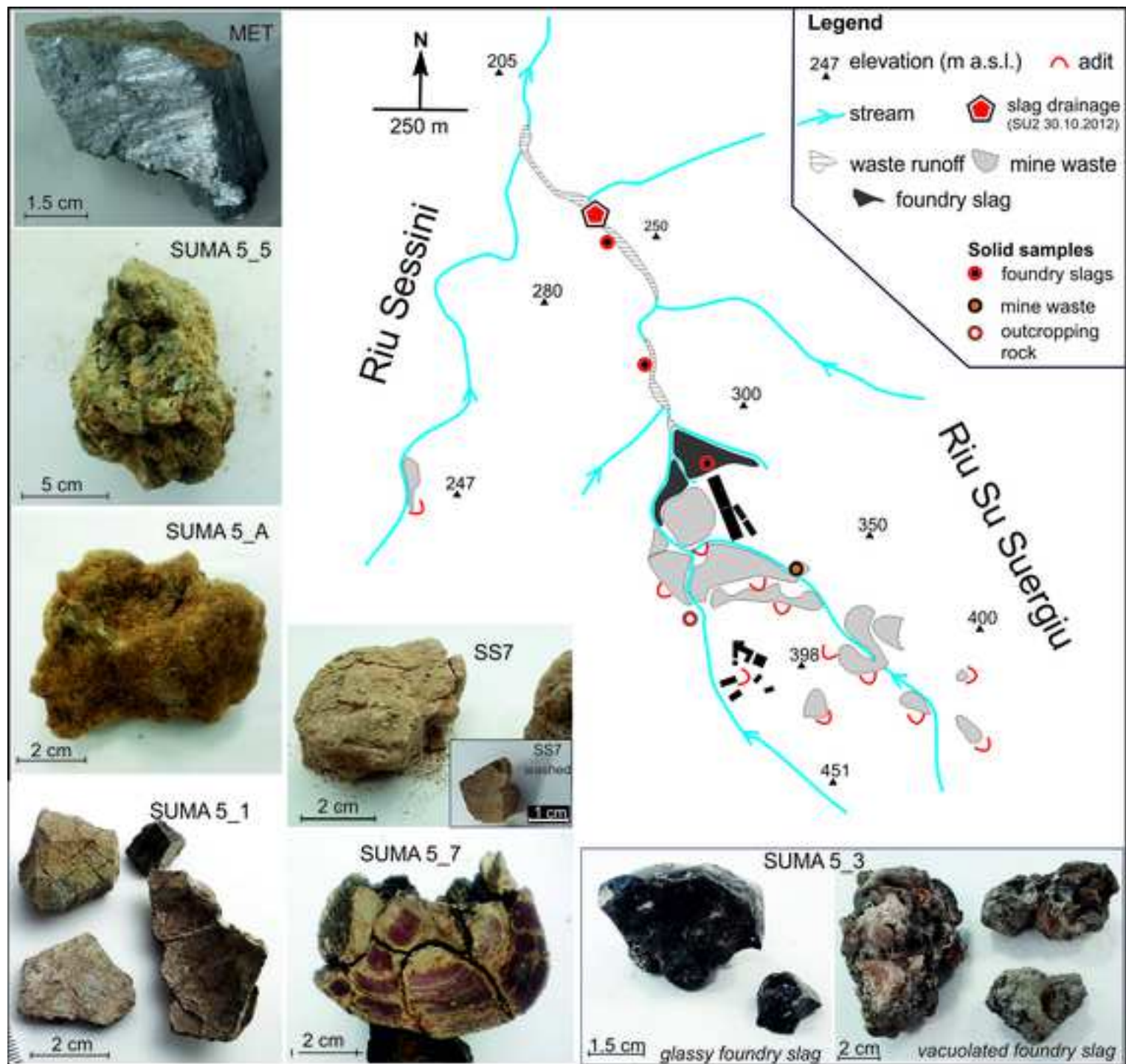
Table 4. Selected analyses of mopungite-like phases from the inner part of the slag fragments.

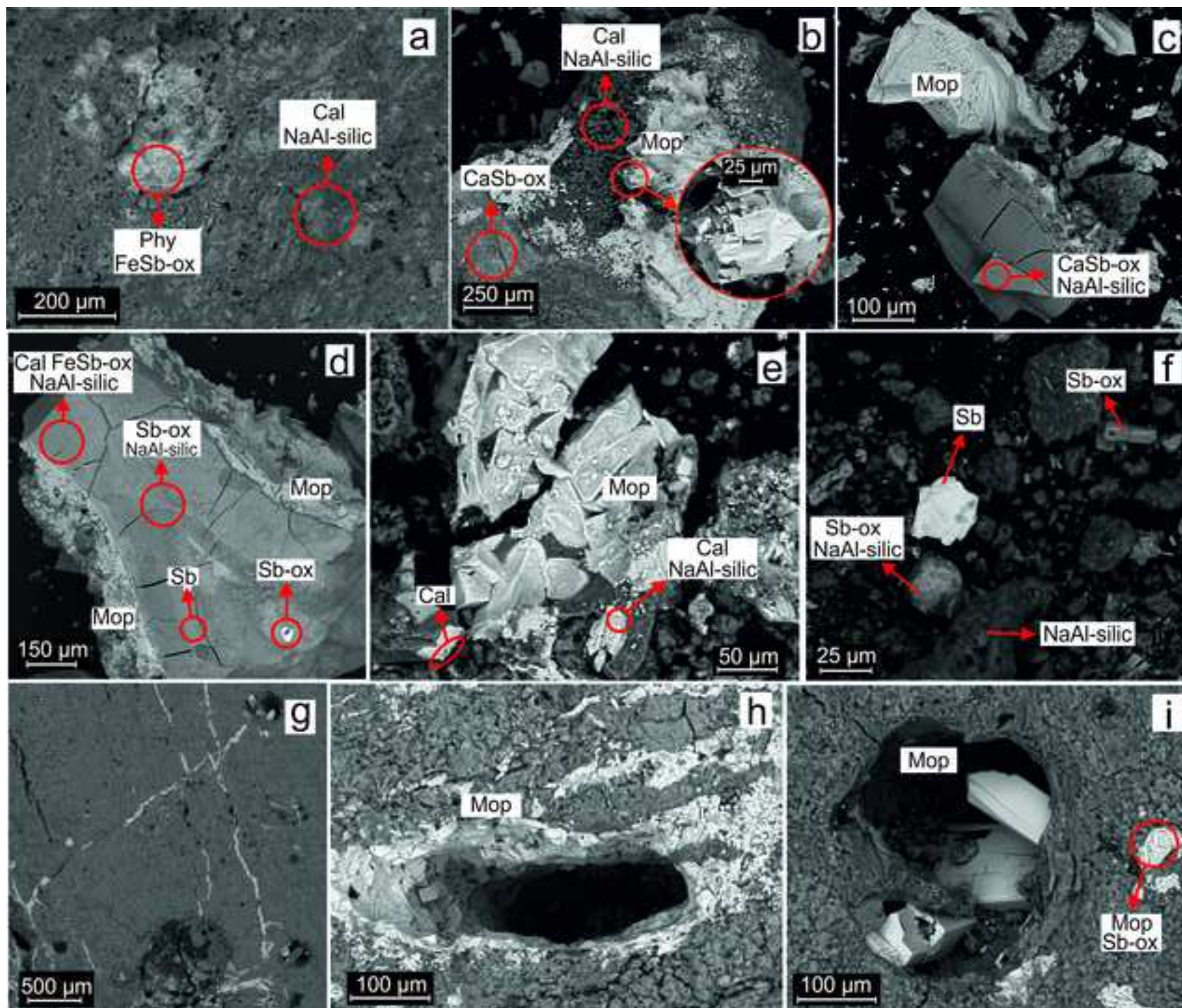
Sample	SUMA_5_4		SS7	SUMA_5_1				
Point analysis	15	16	17	18	19	20	21	22
	Wt ox%							
Na ₂ O	8.79	10.84	7.64	10.33	8.01	11.82	9.71	9.25
Sb ₂ O ₅	79.55	73.99	70.44	74.66	75.58	76.55	77.76	72.10
FeO	0.16	0.11	0.22			0.12	0.09	0.36
SnO ₂	0.32	0.29	0.29	0.30	0.26	0.20	0.21	0.28
SiO ₂	1.62	0.25	0.81	0.46	0.63	1.07	1.12	1.45
ZnO	0.14				0.12	0.21		0.49
Al ₂ O ₃	0.36		0.43				0.11	0.37
MgO	0.06	0.08						0.08
TiO ₂								0.08
WO ₃		0.32	0.31					
K ₂ O	0.03							
Tot	91.03	85.87	80.14	85.74	84.61	89.98	89.00	84.46

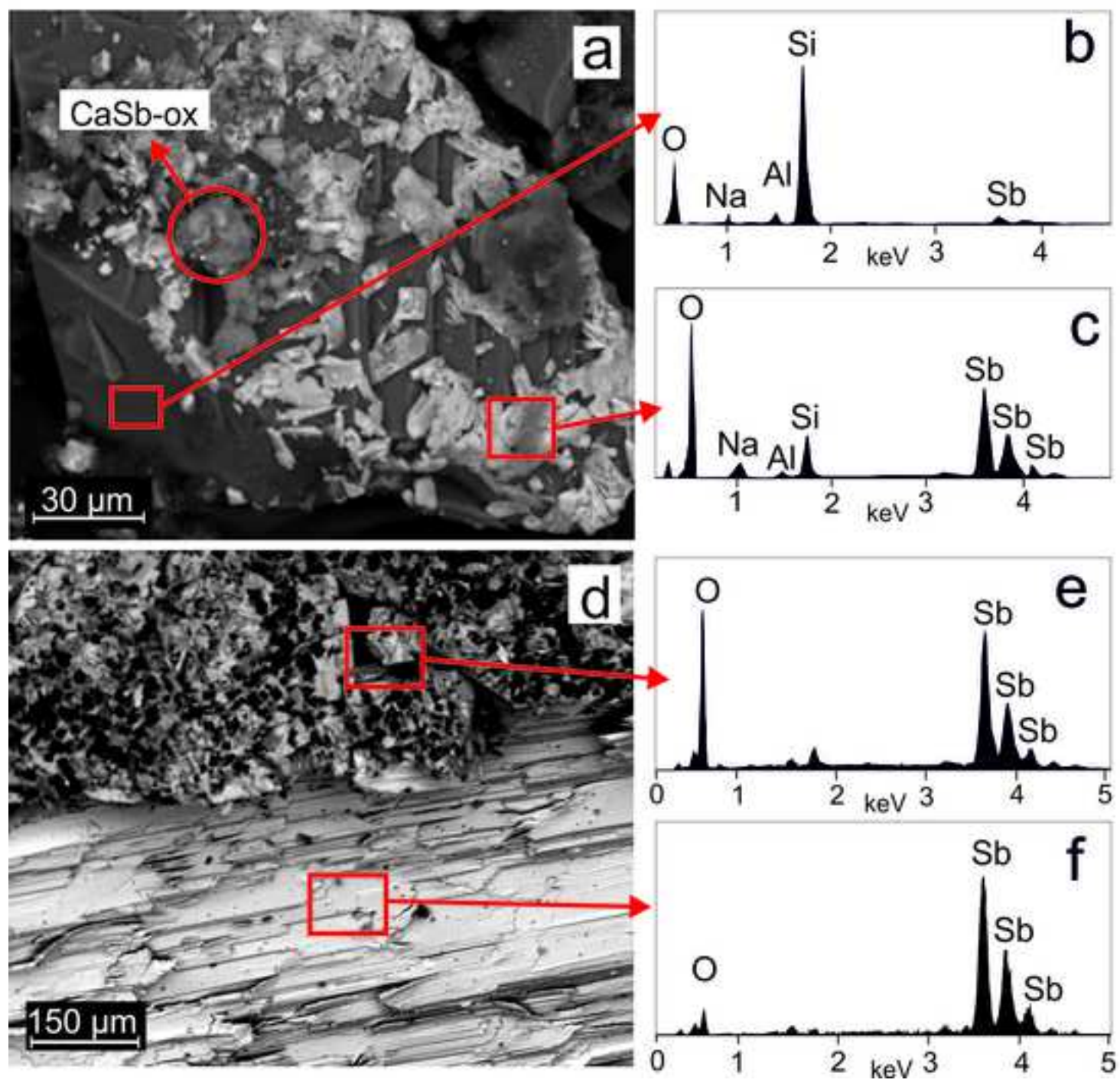
Table 5. Selected analyses of Ca-rich and Na-rich silicates from the slag fragments matrix

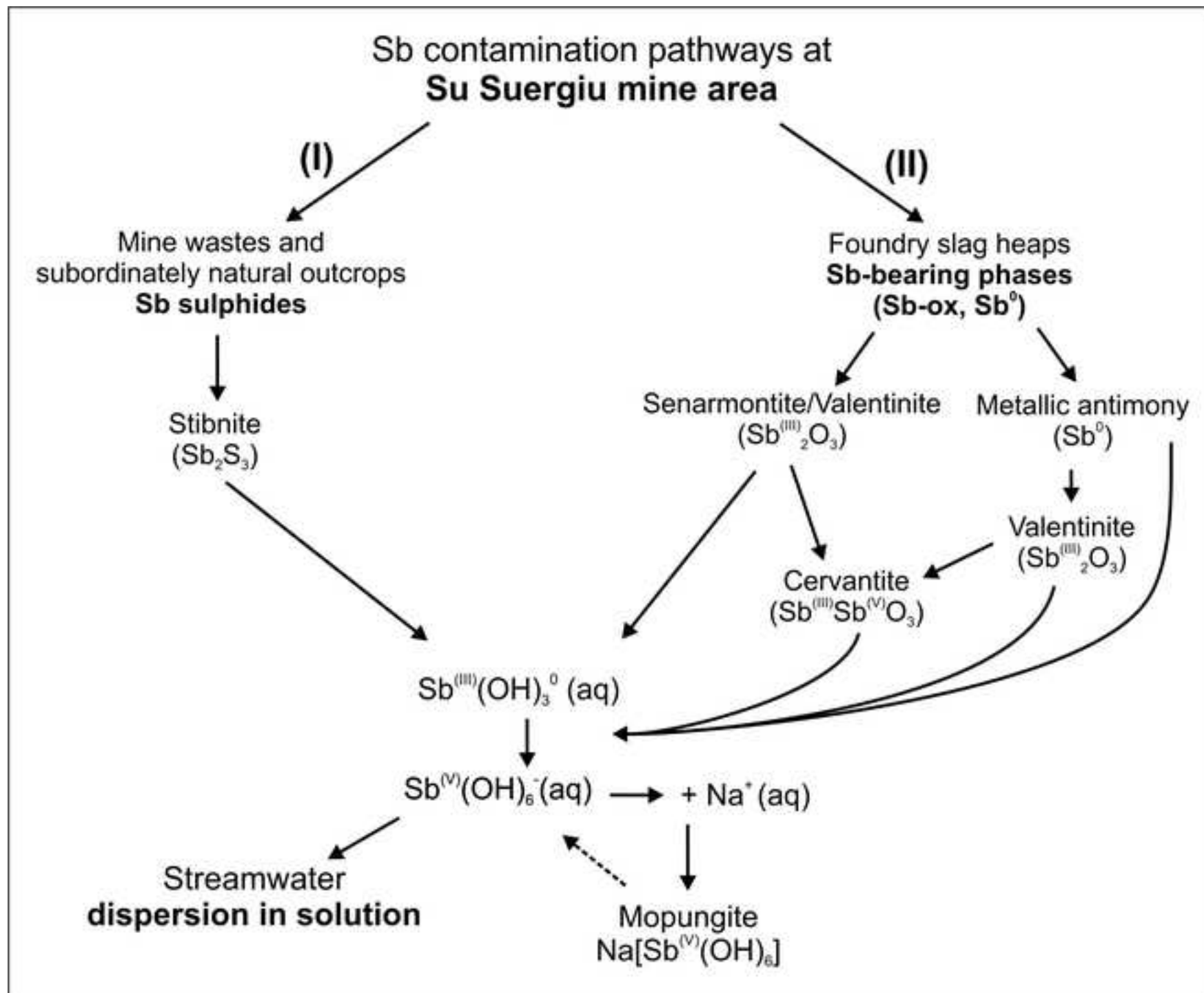
Sample	SUMA-5_4			
Point analysis	*11	*12	**13	**14
	Wt ox%			
SiO ₂	31.32	31.31	40.10	39.48
Al ₂ O ₃	0.06	0.03	27.93	27.38
TiO ₂		0.08		
FeO	0.33	0.26	1.31	1.19
MgO	0.14	0.16	0.12	0.09
CaO	59.13	59.04	0.44	0.09
Na ₂ O	0.20	0.18	19.31	20.46
K ₂ O		0.01	0.26	0.28
ZnO	0.30	0.18	0.09	
NiO	0.06		0.05	
Cr ₂ O ₃		0.05	0.05	
Sb ₂ O ₅	0.44	0.87	0.09	0.15
SnO ₂		0.09		
WO ₃			0.28	
Tot	91.98	92.26	90.02	89.52
* Good match with phases like Hillebrandite [Ca ₆ Si ₃ O ₉ (OH) ₆] or Spurrite [Ca ₅ (SiO ₄) ₂ (CO ₃)]; total oxides at about 92% is acceptable considering 9% of H ₂ O or CO ₂ , respectively				
** Good match with phases like cancrisilite or kyanoxalite, both belonging to cancrinite group; total oxides at about 90% is acceptable considering 6% H ₂ O and 5% CO ₂ .				

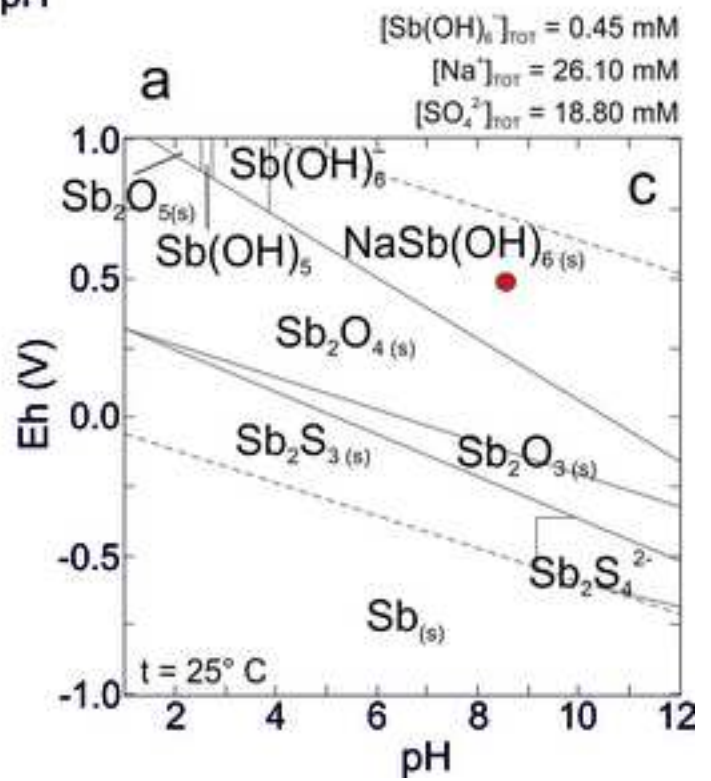
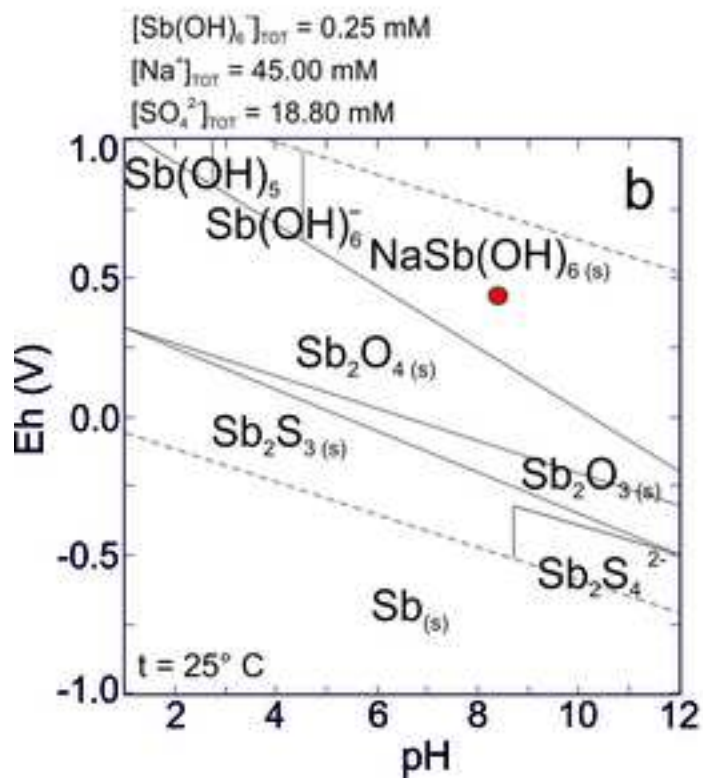
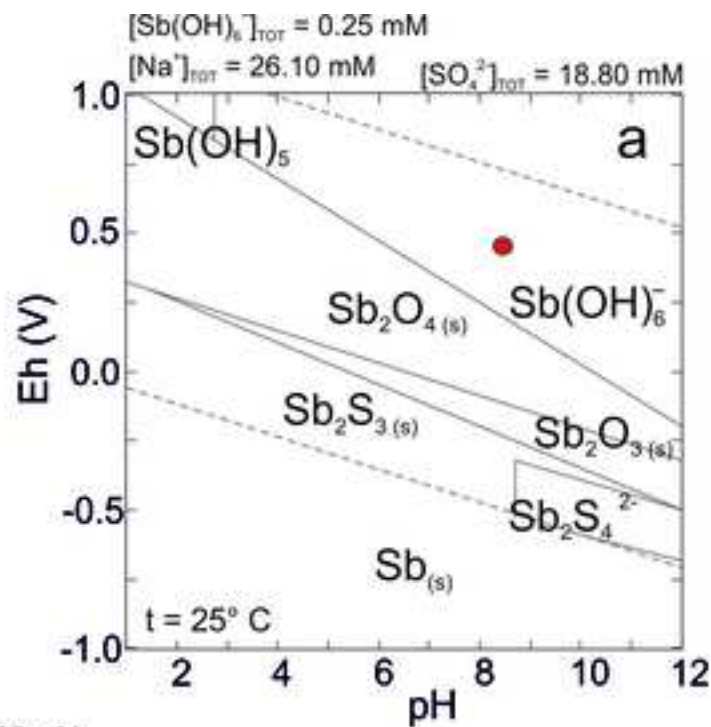












Supplementary Materials

Antimony contamination sources and alteration pathways of Sb mineral phases in an abandoned mining area: the role of secondary mopungite [NaSb(OH)₆]

Dario Fancello^a, Elisabetta Dore^{a*}, Daniela Medas^a, Nicola Rigonat^a, Carlo Meneghini^b, Marilena Moroni^c, Stefano Naitza^a, Patrizia Onnis^d, Giovanni De Giudici^a

^aDepartment of Chemical and Geological Sciences, University of Cagliari, Cittadella Universitaria, Monserrato, 09042, CA, Italy

^bDepartment of Science, Roma Tre University, Rome, Italy

^cDepartment of Earth Sciences, University of Milan, Italy

^dEnvironment & Sustainability Institute and Camborne School of Mines, University of Exeter, Penryn, TR10 9FE, United Kingdom

Correspondence: Elisabetta Dore (elisabetta.dore@unica.it)

Figure S1. XRPD patterns of outcropping rock, mine waste and foundry slags samples. (abbreviations: Cal= calcite; Crs= cristobalite; Dol= dolomite; Gy= gypsum; Hal= halotrichite; Hm= hematite; Hx= hexahydrite; Jar= jarosite; Kal= kalinite; Sb= metallic Sb; Mois= moissanite; Mop= mopungite; Mul= mullite; PbJ= plumbojarosite; Phy= phyllosilicates; Py= pyrite; Qtz= quartz; Sen= senarmonite; Stbn= stibnite; Val= valentinite).

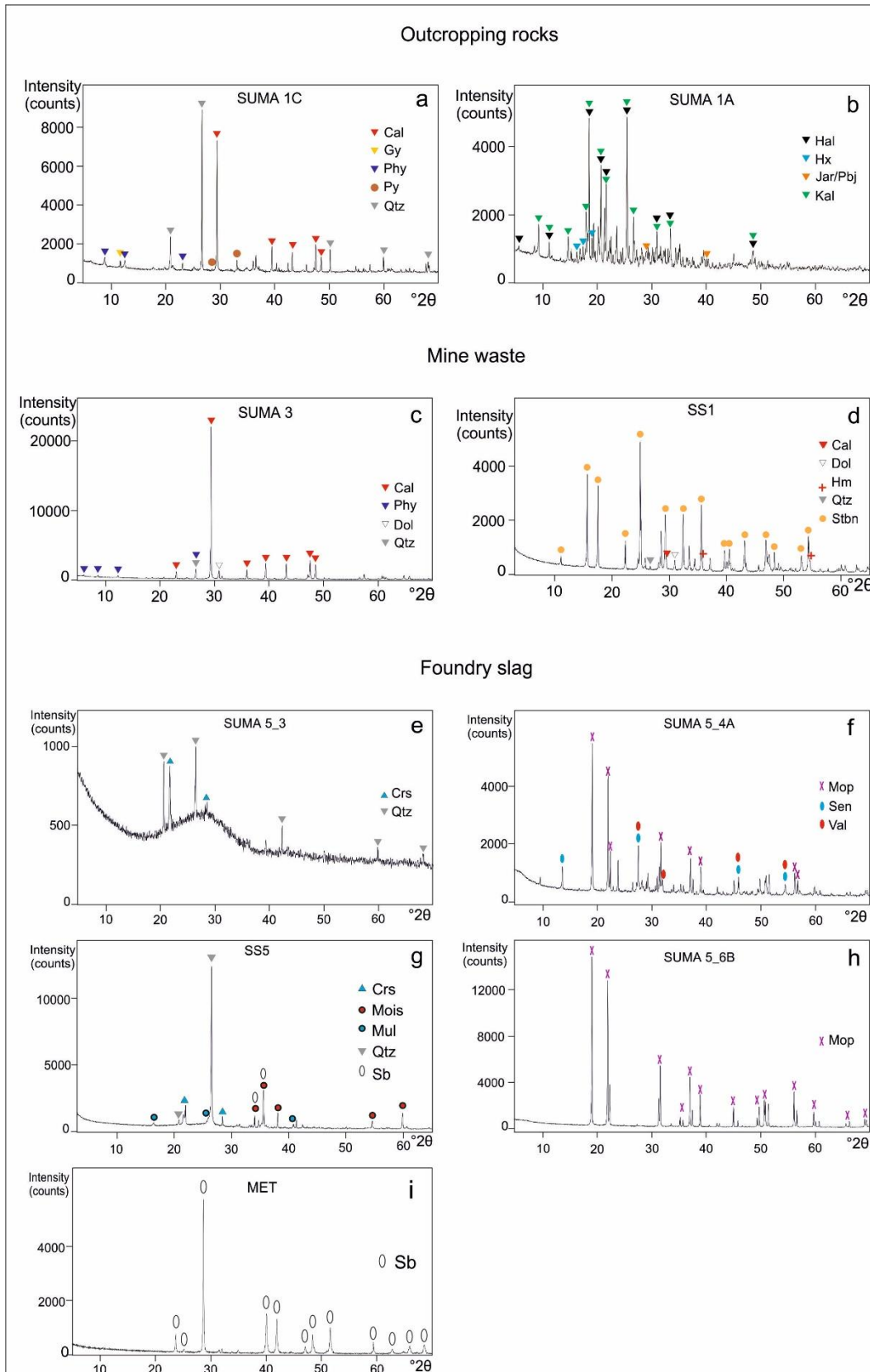


Table S2 List of reflections for the sample SUMA_5_6A (Relative Intensity > 5%).

No.	Pos. [°2Th.]	FWHM [°2Th.]	h	k	l	Mult.	d-spacing [Å]	Rel. Int. [%]
1	11.88363	0.05019	1	1	1	8	4.60380	100
2	13.65477	0.05185	0	2	0	4	4.00924	67.7
3	19.52234	0.05802	0	2	2	8	2.81147	36.2
4	13.88228	0.05207	0	0	2	2	3.94360	27.8
5	22.77805	0.06185	1	3	1	8	2.41398	23.6
6	23.90358	0.06323	2	2	2	8	2.30190	20.1
7	30.94527	0.07253	0	4	2	8	1.78700	18.2
8	31.26120	0.07297	0	2	4	8	1.76939	16.5
9	33.96565	0.07684	2	4	2	8	1.63221	15.5
10	19.35891	0.05784	2	2	0	4	2.83496	14.6
11	34.25668	0.07726	2	2	4	8	1.61875	14.2
12	27.51452	0.06786	0	4	0	4	2.00462	11.6
13	33.96565	0.07684	4	2	2	8	1.63221	10.3
14	30.83931	0.07238	2	4	0	4	1.79299	10.3
15	23.05743	0.06219	1	1	3	8	2.38513	9.7
16	30.28320	0.07161	1	3	3	8	1.82511	6.8
17	30.83931	0.07238	4	2	0	4	1.79299	6.8
18	30.06673	0.07131	3	3	1	8	1.83794	6.7
19	36.01436	0.07986	1	5	1	8	1.54220	6.7
20	30.28320	0.07161	3	1	3	8	1.82511	6.6
21	42.12682	0.08939	4	2	4	8	1.32656	5.6
22	41.21045	0.08792	5	3	1	8	1.35472	5.4
23	44.25653	0.09288	0	6	2	8	1.26571	5.2
24	39.65062	0.08544	0	4	4	8	1.40573	5.2

Table S3 List of reflections for the sample SUMA_5_6B (Relative Intensity > 5%)

No.	Pos. [°2Th.]	FWHM [°2Th.]	h	k	l	Mult.	d-spacing [Å]	Rel. Int. [%]
1	11.87996	0.04753	1	1	1	8	4.60534	100
2	13.64945	0.04860	0	2	0	4	4.01092	69.3
3	19.51808	0.05296	0	2	2	8	2.81231	36.6
4	13.88115	0.04874	0	0	2	2	3.94432	29.6
5	22.77068	0.05587	1	3	1	8	2.41494	23.7
6	23.89720	0.05696	2	2	2	8	2.30267	20.0
7	30.93570	0.06448	0	4	2	8	1.78766	18.4
8	31.25603	0.06485	0	2	4	8	1.76979	16.9
9	33.95476	0.06805	2	4	2	8	1.63282	16.4
10	19.35237	0.05282	2	2	0	4	2.83615	15.2
11	34.24984	0.06841	2	2	4	8	1.61917	14.4
12	27.50478	0.06066	0	4	0	4	2.00546	12.3
13	33.95476	0.06805	4	2	2	8	1.63282	11.0
14	23.05395	0.05614	1	1	3	8	2.38567	10.6
15	30.82826	0.06436	2	4	0	4	1.79374	10.2
16	30.27587	0.06372	3	1	3	8	1.82567	7.2
17	30.27587	0.06372	1	3	3	8	1.82567	7.1
18	36.00156	0.07058	1	5	1	8	1.54283	6.6
19	30.82826	0.06436	4	2	0	4	1.79374	6.4
20	30.05638	0.06348	3	3	1	8	1.83869	6.2
21	42.11586	0.07858	4	2	4	8	1.32697	5.5
22	41.19549	0.07733	5	3	1	8	1.35528	5.4
23	39.64093	0.07526	0	4	4	8	1.40615	5.2
24	44.24112	0.08150	0	6	2	8	1.26621	5.1

Figure S4 BSE images of samples analysed by EMP with the exact position of selected spot analyses reported in Tables 3, 4 and 5. Each image is labelled with the name of the sample it belongs to.

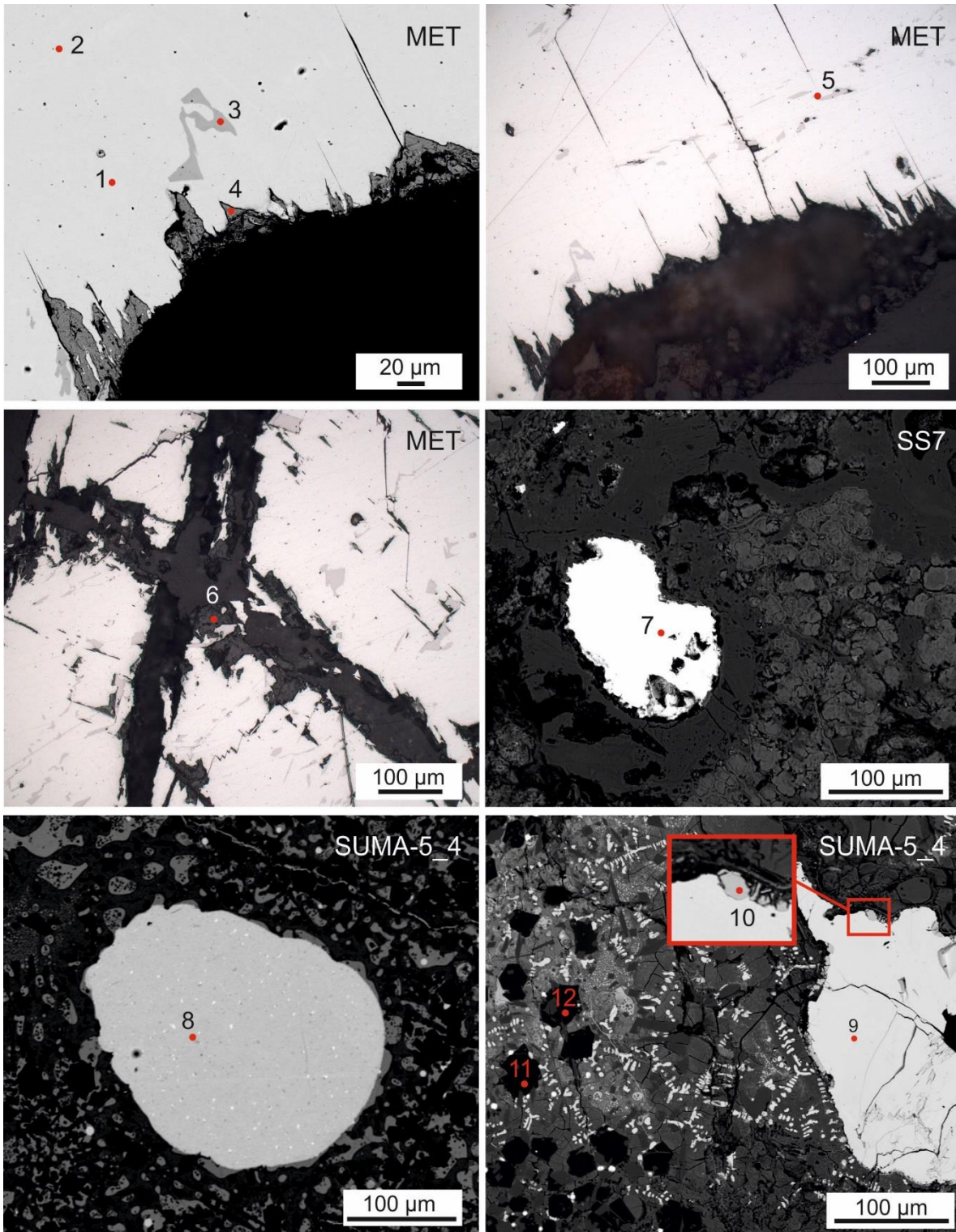


Figure S5 BSE images of samples analysed by EMP with the exact position of selected spot analyses reported in Tables 3, 4 and 5. Each image is labelled with the name of the sample it belongs to.

